Master Thesis
Physics

Rheinisch-Westfälische Technische Hochschule Aachen

III. Physikalisches Institut B

Detection and Analysis of Recombination Rates during Electron Cooling at COSY

Mathis Beyß

October 30, 2019

Declaration of Authorship

I hereby declare that the thesis submitted is my own unaided work. All direct or indirect sources used are acknowledged as references.

I am aware that the thesis in digital form can be examined for the use of unauthorized aid and in order to determine whether the thesis as a whole or parts incorporated in it may be deemed as plagiarism. For the comparison of my work with existing sources I agree that it shall be entered in a database where it shall also remain after examination, to enable comparison with future theses submitted. Further rights of reproduction and usage, however, are not granted here.

This paper was not previously presented to another examination board and has not been published.

_____   _____
(City, Date)   (Mathis Beyß)

The Thesis has been carried out under the supervison of:

1. Examiner:	**Prof. Dr. Jörg Pretz**	(RWTH Aachen)
2. Examiner:	**Prof. Dr. Achim Stahl**	(RWTH Aachen)

The thesis has been carried out at the Nuclear Physics Institute (IKP-2) of the
Forschungszentrum Jülich GmbH

JÜLICH
Forschungszentrum

Abstract

At the COoler SYnchrotron at the Forschungszentrum Jülich, electron cooling is used to shrink the emittance of proton and deuteron beams for high precision experiments. Neutral particle detectors consisting of two plastic scintillators are used to observe the electron-ion recombination rate during electron cooling of the proton beam. The recombination rate provides valuable information on the transverse temperature of the electron beam. A detailed analysis allows to determine the cause of a heating-up of the electron beam.

Using FPGAs and a System-on-a-Chip approach a fast data acquisition and processing system of the detector signals has been set up and integrated into the Experimental Physics and Industrial Control System (EPICS). Besides a web monitoring system for real-time diagnostics utilizing the WebSocket protocol together with EPICS Channel Access is presented.

Acknowledgement

Contents

List of Figures

List of Tables

1. Introduction

Since the first working particle accelerator was built by Ernest O. Lawrence as part of the Manhattan Project in 1931, particle accelerators play an important role not only in fundamental research of particle physics. It is estimated that currently there are around 30,000 particle accelerators located across the globe. Many of them are used in a wide variety of applications beyond physics research. For instance in medicine particle accelerators allow radiation treatment of patients, that developed cancer, but also in technology smaller accelerators are used for ion implants in the manufacturing of semiconductor devices such as computer chips.

Experiments in fundamental research often require high quality beams. Beam cooling allows to shrink the emittance and therefore increase the lifetime of a particle beam. One implementation of beam cooling is the so called electron cooling. In this method the particle beam is superimposed by a "cool" electron beam. Through coulomb interaction the particle beam can transfer its inner energy to the electron beam, which leads to a shrinking emittance of the particle beam.

When working with ion beams such as proton or deuteron beams, ions occasionally recombine with the cooling electrons leaving a neutral particle behind, which can be separated from the ion beam and detected. Such recombined electron-ion pairs provide valuable information on the cooling process.

Nowadays, electron coolers are also used to specifically study the nature of recombination processes. Specially due to their complex electronic structure recombination processes such as dielectric recombination of more complex ions are not understood in detail yet. Thus electron coolers also find use in applications apart from particle beam cooling.

Nevertheless, for a detailed analysis of recombination processes a precise detection system is of high importance. Modern devices like FPGAs together with standard scintillator technology offer easy to implement detection systems.

The present thesis deals with the detection and analysis of recombined electron-ion pairs during electron cooling. It basically consists of two main parts: The first part describes the detector system for recombined particles and the novel data acquisition and monitoring system, that has been developed in the course of this work. The second part of the thesis takes a closer look into the analysis of the gathered data and shows up valuable insights of the electron cooling process, that can be gained from recombined particles. Finally, based on the former analysis suggestions to optimize the electron cooling process are pointed out.

1.1. **Cooler Synchrotron COSY**

The *Nuclear Physics Institute* (IKP) at the *Forschungszentrum Jülich* is running the *Cooler Synchrotron* (COSY) for fundamental research in the field of hadron, particle and nuclear physics. The particle accelerator and storage ring *COSY* provides unpolarized as well as polarized proton and deuteron beams in the momentum range from 200 MeV/c up to 3.7 GeV/c. Currently carried out experiments are amongst others the *Electric Dipole Moment Measurement* (EDM) and machine and detector studies for the *Facility for Antiproton and Ion Research* (FAIR).

As one of a few particle accelerators in the medium energy range *COSY* provides both electron and stochastic cooling. For this purpose two different electron coolers are installed on each straight section within in the storage ring. The *2 MeV electron cooler* (2 MeV-Cooler) positioned directly after the injection beam line allows transverse as well as longitudinal beam cooling with electron energies between 25 keV and 2 MeV. The *100 keV electron cooler* (100 keV-Cooler) positioned on the opposite straight section provides beam cooling with electron energies in the range from 25 keV up to 100 keV range.

For an optimization of the beam cooling during operation the monitoring and analysis of recombined electron-ion-pairs is vital.
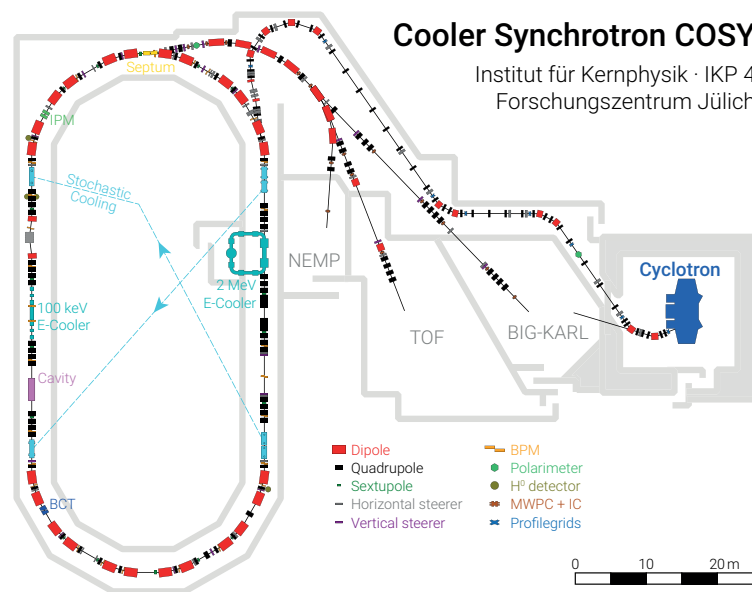
Figure 1.1.: Overview of the accelerator facility at the *Forschungszentrum Jülich*

1.2. 100 keV Electron Cooler

The 100 keV-Cooler was commissioned in the year 1992 and allows the electron cooling of either proton beams up to a kinetic energy of 184 MeV or deuteron with an maximum kinetic energy of 367 MeV. The most important parameters of the 100 keV-Cooler can be found in table 1.1.

A cross section of the 100 keV-Cooler can be seen in figure 1.2. Inside the electron gun, electrons are released from an 1000°C hot dispenser cathode made out of barium oxide and accelerated electrostatically by NEC tubes to their final velocity. Electrons afterwords are guided starting from the electron gun through the cooling section to the collector by a guiding magnetic field. Finally inside the collector the electron beam will be decelerated by a deceleration column down to a few keV. The function of the collector is to gather electrons with a high efficiency, because lost electrons become a burden on the stability of the high voltage power supply and can give rise to gas sources in the vacuum chamber.

The guiding field is formed by solenoid and toroid magnets arranged in the shape of an upright U. Two 35°- and 55°-toroids forming two 90° bends establish the link between the gun- and collector-solenoid with the drift-solenoid respectively. Different outer radii of the 35°- and 55°-toroids allow the insertion of the ion beam in between. During electron cooling all magnets are connected in series and can be driven at the same magnetic field strength up to 132 mT. Currently a guiding field of 50 mT is in use.
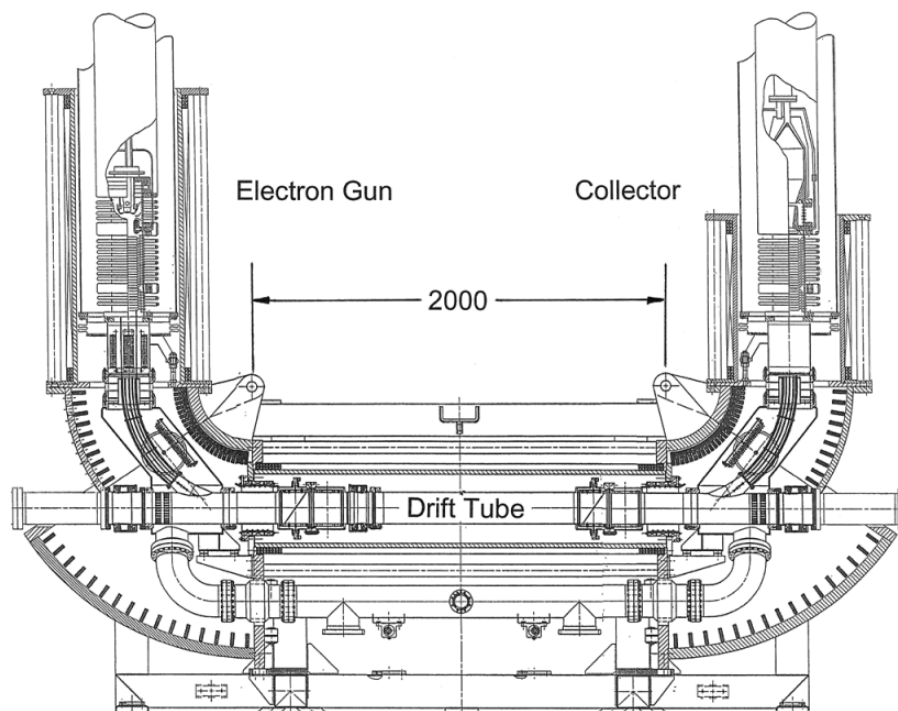
Figure 1.2.: Cross section of the 100 kev electron cooler [37]

A uniform magnetic field is important to obtain an electron beam with a low transverse temperature. Maximal deviations in the field strength arise at the intersection of solenoids and toroids from missing turns at the edges of the coils [37]. Three transition solenoids (gap-solenoids) in addition compensate the field errors at the transition points to avoid a heating-up of the electron beam.

At each straight section a pair of Helmholtz coils is wrapped around the solenoids. Those correction coils can be controlled to adjust the electron directory in the horizontal and vertical direction.

The 100 keV-Cooler as well is surrounded by two steerer magnets on each site to align the ion beam inside the electron cooler and to compensate the orbit disruption caused by the guiding field inside the toroids.

100 keV Electron Cooler Parameters	
Cooling Length	2.0 m
Electron Beam Diameter	0.0254 m
Electron Beam Radius in Toroids	0.6 m
Maximum Electron Beam Current	4.0 A
Maximum Electron Beam Voltage	100 kV
Cathode Temperature	~ 1000°C

Table 1.1.: Relevant parameters of the 100 keV electron cooler [41]

2. Theory

The later analysis of recombination rates builds on a basic understanding of electron cooling and the recombination process itself. The following chapter provides an introduction to the process of magnetized electron cooling and the important properties of an electron beam. In addition, a description of radiative recombination and the dependence of the recombination process on the temperature of electron beam will be given.

2.1. Principles of Beam Cooling

The purpose of beam cooling is the reduction of the phase space volume occupied by the particle beam. In this way one is able to achieve a beam quality needed for high precision experiments. In addition heating effects due to internal target can be compensated which leads to a significantly longer beam lifetime.

The process of beam cooling does not follow the *Liouvilles Theorem* which states that "in a system where the particle motion is controlled by external conservative forces the phase space density is conserved" [38]. Therefore the cooling of a particle beam is a non-Liouvillean process since it violates the assumption of conservative forces to reduce the emittance of the particle beam.

There are different ways to cool a particle beam. The main methods are:

- stochastic cooling

- electron cooling

- ionization cooling

- laser cooling

In the following the basic principle of electron cooling will be explained in more detail.

2.2. Introduction to Electron Cooling

The first experiments on electron cooling were carried out by G. Budker at the *Institute of Nuclear Physics in Novosibirsk* in the 1970s based on his ideas of "an efficient method to damp particle oscillations in proton and antiproton storage rings", which

he already suggested in the year 1967 [22][8].

Generally a particle beam can be considered as an ion plasma that is circulating in the storage ring. The temperature of the ion plasma is defined as the energy spread of the ions in the center-of-mass-frame.

During the process of electron cooling the particle beam is merged with a quasi mono-energetic electron beam for a certain length of the storage ring circumference. The electron beam is having the same velocity than the ion beam. In this case the relative velocity between ions and electrons is just affected by the energy spread inside both the ion and the electron beam or in other words the temperature of both beams.

Now due to low relative velocities in the co-moving frame electrons and ions interact via Coulomb collision. By Coulomb collision momentum is transferred from the "hot" ion beam to the "cold" electron beam approaching the thermodynamic equilibrium. The electron beam though is constantly regenerated by the electron gun and therefore preserves its temperature. Ion and electron beam will exchange momentum until both have the same temperature.

Since electron beam and ion beam are travelling with the same velocity their kinetic energy should just be dependent on their mass relation:

$$\frac{E_i}{E_e} = \frac{m_i}{m_e},\tag{2.1}$$

where E_i and E_e represent the kinetic energy and m_i and m_e the mass of ions and electrons. For electron energies of $100\,\mathrm{keV}$ as they are possible with the $100\,\mathrm{keV}$-Cooler of COSY one is able to cool either protons with a kinetic energy of up to $184\,\mathrm{MeV}$ or deuterons with a kinetic energy of up to $367\,\mathrm{MeV}$. The beam cooling can either be initiated after injection of the ion beam into the storage ring or after the acceleration to their final energy.
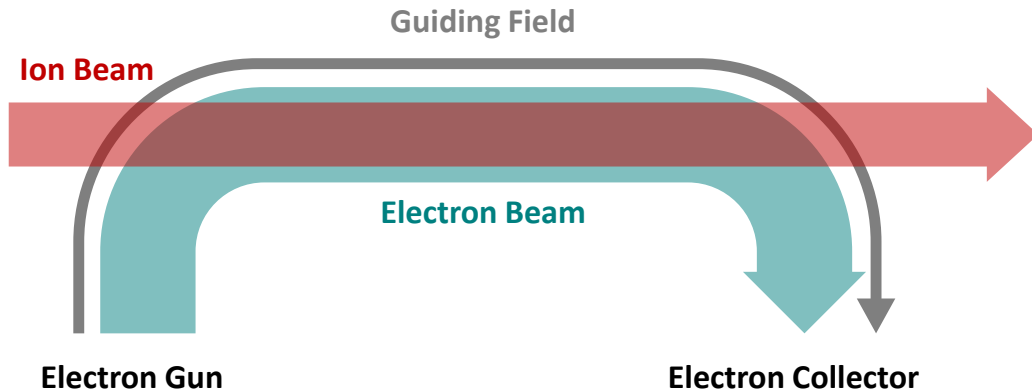
Figure 2.1.: Schematic representation of electron cooling

2.2.1. Properties of the Electron Plasma

As already mentioned, the electron beam, needed for the cooling process is produced by an electron gun. In an electron gun electrons are released in a current carrying cathode by *thermionic emission*. Meaning the thermal energy given to the electrons in the cathode exceeds the work function of the cathode material. This gives rise to a current flow of electrons at the surface from the cathode material into the vacuum. The initial state of the electron plasma accumulating around the electron gun is fully determined by the temperature of the cathode T_c and follows a Maxwellian distribution:

$$f\left(v\right) = \left(\frac{m_e}{2\pi k T_c}\right)^{2/3} \exp\left(-\frac{m_e v^2}{2k T_c}\right), \tag{2.2}$$

where $v = |\vec{v}|$ is the absolute electron velocity and m_e the electron mass. The Boltzmann constant k makes a connection between the temperature of a gas and its internal energy. When the temperature of a beam is mentioned during this thesis it always refers to the internal energy kT.

In the following the electron plasma is accelerated towards the cooling region. The electrostatic acceleration of the electron beam leads to a reduction of the relative velocity spread by several orders of magnitude parallel to the direction of acceleration. However, the transverse velocity spread of the electron beam stays unchanged, because the transverse and parallel velocity components do not depend on each other. Under the assumption that the parallel velocity distribution of the electrons is still Maxwellian distributed after acceleration one can write the overall distribution as a product of both:

$$f\left(v\right) = \frac{1}{(4\pi)^{2/3}\Delta_\parallel \Delta_\perp^2} \exp\left(-\frac{v_\parallel^2}{\Delta_\parallel^2} - \frac{v_\perp^2}{\Delta_\perp^2}\right). \tag{2.3}$$

Here $\Delta_\parallel$ and $\Delta_\perp$ represent the longitudinal and transverse root mean square (rms) of the electrons and $v_\parallel$ and $v_\perp$ their velocity. Using the rms one is able to state the definition of the temperature of a gas as its energy spread in the center-of-mass-frame:

$$kT = \frac{m_e}{2}\Delta^2. \tag{2.4}$$

In the transverse direction the rms just depends on the cathode temperature and is therefore given by:

$$\Delta_\perp = \sqrt{\frac{2k T_c}{m_e}}, \tag{2.5}$$

This implies, that the transverse electron temperature in a first approximation is equal to the temperature of the cathode $kT_\perp = kT_c$. The longitudinal temperature on the other hand shrinks down due to the acceleration of the beam. To understand this behaviour one first needs to find an expression for the longitudinal rms $\Delta_\parallel$ of the

electron beam.

The kinetic energy of the beam E_e can be expressed through

$$E_e = (\gamma - 1)mc^2 \approx \frac{\beta^2}{2}m_ec^2, \tag{2.6}$$

where for low energies one can expand the gamma function $\gamma \approx 1 + \beta^2/2$. The energy of electrons varies with the temperature of the cathode $\sigma_E = kT_c$. One can derive the parallel rms by comparing the relative energy spread σ_E/E_e with the relative velocity spread $\Delta_\parallel/\beta c$ of the electrons. The relative energy spread needs to be twice as large as the relative velocity spread:

$$\frac{\sigma_E}{E_e} = \frac{2\Delta_\parallel}{\beta c} \quad \Longrightarrow \quad \Delta_\parallel = \frac{kT_c}{\beta m_e c}. \tag{2.7}$$

Insertion of the parallel rms into equation 2.4 results in a longitudinal temperature of

$$kT_\parallel = \frac{k^2T_c^2}{2\beta^2c^2m_e} = kT_c \cdot \frac{kT_c}{4E_e}. \tag{2.8}$$

As it can be seen, the parallel temperature scales with the relative energy spread, hence the ratio of the cathode temperature kT_c and the kinetic energy of the electron beam E_e. This indicates the more the electron beam will be accelerated the more the longitudinal temperature of the beam decreases.

In a second approximation Coulomb repulsion between electrons can lead to an increase of the beam temperature. This effect is mainly of importance at high electron densities. The Coulomb potential between two electrons V_{ee} is described the formula:

$$V_{ee}(\bar{r}) = \frac{2e^2}{4\pi\epsilon_0\bar{r}} = 2m_ec^2\frac{r_e}{\bar{r}}, \tag{2.9}$$

where the classical electron radius r_e was introduced at this point. Even though according to today's understanding electrons are point-like particles with no spatial extent, the classical electron radius is an useful quantity to characterize electron interaction on a microscopic scale. $\bar{r}$ denotes the average electron distance in the beam. The average distance of the electrons can be estimated with help of the electron density n_e. Under the assumption that the electrons are equally distributed and the electron beam has a cylindrical shape the electron density is given by

$$n_e = \frac{I_e}{e\beta c\pi r_c^2}, \tag{2.10}$$

where r_c is the radius of the cathode and I_e the electron current measured at the collector of the electron cooler. The average electron distance subsequently is estimated by $\bar{r} = n^{-1/3}$.

2.2.2. Magnetized Cooling

Electrons surrounded by an uniform magnetic field are following the magnetic field lines on a helical orbit. Reason for this is the Lorentz force that is always directed perpendicular to the magnetic field lines. The *Lamor radius* of the electrons can be defined as follows:

$$r_L = \frac{m_e v_\perp}{eB},\tag{2.11}$$

where $v_\perp$ depicts the transverse electron velocity.

In order to overcome the effect of Coulomb repulsion a sufficiently large magnetic field along the electron beam trajectory has to be applied [29]. The guiding field B has to have a field strength, such that the average Lamor radius of the electrons is much smaller than the average distance between them:

$$r_L = \frac{m_e v_\perp}{eB} < \bar{r} \quad \Longrightarrow \quad B > \frac{n_e^{1/3}\sqrt{kT_c m_e}}{e}.\tag{2.12}$$

To gain a better picture for the field strength, that has to be applied, figure 2.2 shows the minimal guiding field strength for different electron beam currents at injection and maximal energy available in the 100 keV-Cooler. For a typical beam current of 250 mA one has to apply a magnetic field of at least 24 mT in order to compensate the effect of Coulomb repulsion. Currently a guiding field of 50 mT for all beam energies is used.

The small increase of the guiding field strength for a lower kinetic energy is due to the fact, that with a lower beam velocity one has to increase the electron density in order to receive the same beam current. A denser electron beam requires a stronger guiding field to avoid a heating-up. The guiding field is normally produced by solenoid and toroid magnets surrounding the the electron cooler.
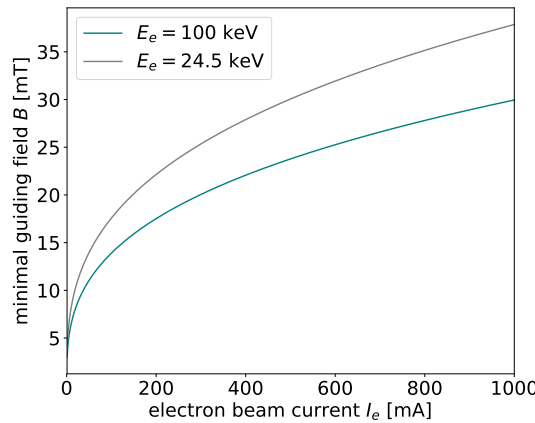
Figure 2.2.: Minimal guiding field as a function of the electron beam current

2.2.2.1. Adiabatic Beam Expansion

In a spatially constant guiding field the transverse temperature of the electron beam stays constant. Now one can assume electrons are travelling from an region with a higher magnetic field to a region with a lower field. This in principal can be done with two solenoid magnets in a row, where the first one is driven at a higher current as the second one. In such a setup the spatial reduction of the field strength leads to a divergence of the guiding field lines. Nevertheless the electrons will still perform motion around the guiding field lines. The divergency of the field lines therefore gives rise to a longitudinal acceleration. To ensure energy conservation an increase in the longitudinal energy needs to lead to a decrease in the transverse energy of the electrons. Accordingly the transverse electron temperature decreases and thereby the whole electron beam cools down. More formally the transverse electron temperature $T_\perp$ divided by the magnetic field strength of the guiding field B needs to be adiabatically invariant:

$$\frac{T_\perp}{B} = \text{const.} \tag{2.13}$$

By introducing the adiabaticity coefficient χ one can define a condition the spatial shift of the magnetic field has to satisfy in order for the beam to expand adiabatically:

$$\chi = \frac{\lambda_L}{B} \left\| \frac{dB}{dz} \right\|. \tag{2.14}$$

A transition therefore is assumed to be adiabatic, if the change of the magnetic field within one cyclotron wavelength of the electron $\lambda_L = 2\pi\sqrt{2m_e E_e}/eB$ is small compared to the strength of the guiding field. In the case of an adiabatic transition the adiabaticity coefficient $\chi \ll 1$. Assuming the strength of the guiding field is reduced from its initial value B_c to an final value B, making use of equation 2.13 one can find an expression for the final transverse electron temperature $T_\perp$ as well as for the final electron beam radius r:

$$T_\perp = \frac{B}{B_c} T_c \quad \text{and} \quad r = r_c \sqrt{\frac{B_c}{B}}. \tag{2.15}$$

As it can be seen in equation 2.15 a decrease of the field strength in the guiding field leads to an reduction of the transverse temperature by the the same factor. The increase in the longitudinal energy mentioned above is negligible at higher beam momenta and therefore does not have an impact on the longitudinal beam temperature. Meanwhile the profile of the electron beam increases by the same factor.

2.3. Radiative Recombination

During electron cooling of a positive charged ion A^{Z^+} different recombination processes can take place. One of the most important is known to be radiative recombination (RR), which is the time reversed process of photoionization. In RR an ion captures a free electron under the emission of a photon with a certain energy $h\nu$:

$$A^{Z^+} + e^- \rightarrow A^{(Z-1)^+} + h\nu, \tag{2.16}$$

with the photon energy $h\nu = E + E_n$. Here E denotes the energy of the free electron and E_n the binding energy of the final state the electron is captured in. Generally in non fully stripped ions other recombination processes like dielectric recombination can take place as well. Since these processes are not of relevance for protons and deuterons studied at COSY, they will not be discussed further at this point. The probability for an electron to be captured by an ion can be expressed by the rate coefficient.

2.3.1. Rate Coefficient

The rate coefficient of a certain recombination process can be derived with the help of its cross section. H.A. Kramers derived the cross section for RR already in 1923 using semiclassical arguments [23]. Since at that time a quantum theory of radiation was not developed yet Kramer made use of Bohr's correspondence principle [3].
In the following years theoretical work has been carried out to find an analytical expression using a quantum mechanical argumentation. A general description was given by M. Stobbe in 1930 making analytical calculation for the cross section of radiative recombination into an arbitrary (n, l) state possible [39].
Later it was shown by Bethe and Salpeter that the same result from Kramers can be obtained from quantum mechanical calculations in the limit of higher states n [7]. Thus a free electron with the energy E in the ion resting frame is captured into a certain energy level n with the cross section [47][28]:

$$\sigma_n(E) = \frac{32\pi}{3\sqrt{3}}\alpha^3 a_B^3 \frac{Z^4 R^4}{nE(Z^2R + n^2E)}, \tag{2.17}$$

where $R \approx 13.6\,\text{eV}$ is the Rydberg energy, α the fine structure constant and a_B the Bohr radius. The initial charge of the ion in units of the elementary charge is again denoted by Z. For small relative energies $E \ll Z^2R/n^2$ the cross-section varies with $1/(nE)$. For the radiative recombination during electron cooling ($E < 1\,\text{eV}$) this implies that the contributions from capture into highly excited Rydberg states decrease quite slowly as n increases.
The results of the cross section for the capture into semiclassical hydrogenic states, lie close to the exact quantum mechanical results. In order to get the exact results corrections must be applied in the upper formula when calculating the cross section for a specific energy level n in the form of the Gaunt factor. This factor represents the

ratio of the exact quantum mechanical calculations by Stobbe and the semiclassical calculations by Kramers [3]. For the calculation of an of a level independent cross section corrections must not be applied.

By summing up the cross sections of all individual energy states one finds the total cross section for an electron to be captured under the emission of radiation

$$\sigma_{tot}(E) = \sum_{n=1}^{n_{str}} \sigma_n(E), \tag{2.18}$$

where n_{str} represents the maximum energy state that may be evidenced in the neutral particle detector. For theoretical considerations one can proceed with $n \to \infty$. However, for experimental implementations one cuts the sum at a certain level n_{str}, because electron-ion pairs recombined into higher excited states $n > n_{str}$ easily get field ionized by a motional electric field when passing the dipole magnets of the storage ring (see subsection 2.3.2). The rate coefficient α_{rr} basically describes the probability for a single ion and electron to recombine into a bound state. It can be derived by calculating the average of the cross section times the velocity of the electrons in the ion-resting-frame:

$$\alpha_{rr} = \langle v\sigma_{tot}(E) \rangle. \tag{2.19}$$

The average can be calculated by integration with respect to the velocity distribution of the electrons:

$$\int_{\mathbb{R}^3} v\sigma_{tot}(E)f(v)\mathrm{d}^3v, \tag{2.20}$$

where $f(v)$ represents the velocity distribution. As it has been shown in subsection 2.2.1 the velocity distribution of the electrons in the center-of-mass frame can be described by an asymmetric Maxwellian distribution:

$$f(v) = \frac{(m_e/2\pi)^{3/2}}{kT_\perp\sqrt{kT_\parallel}} \exp\left(-\frac{m_e v_\perp^2}{2kT_\perp} - \frac{m_e v_\parallel^2}{2kT_\parallel}\right), \tag{2.21}$$

where $v_\parallel$ and $v_\perp$ are the longitudinal and transverse velocities and $kT_\parallel$ and $kT_\perp$ the longitudinal and transverse temperatures of the electron beam, respectively. When discussing the recombination process in the context of electron cooling, the longitudinal temperature is much lower than the transverse ($kT_\parallel \ll kT_\perp$), because the longitudinal velocity spread of the electrons is drastically reduced by electrostatic acceleration (see subsection 2.2.1). Approximating the longitudinal velocity distribution with a delta function one obtains the so called "flattened" Maxwellian distribution:

$$f(v) = \frac{m_e}{2\pi kT_\perp} \exp\left(-\frac{m_e v_\perp^2}{2kT_\perp}\right) \cdot \delta\left(v_\parallel\right). \tag{2.22}$$

M. and J. S. Bell already calculated the recombination coefficient for the capture of electrons by protons ($Z = 1$) in the limit $n \to \infty$ using a normal and "flattened" Maxwellian distribution [6]:
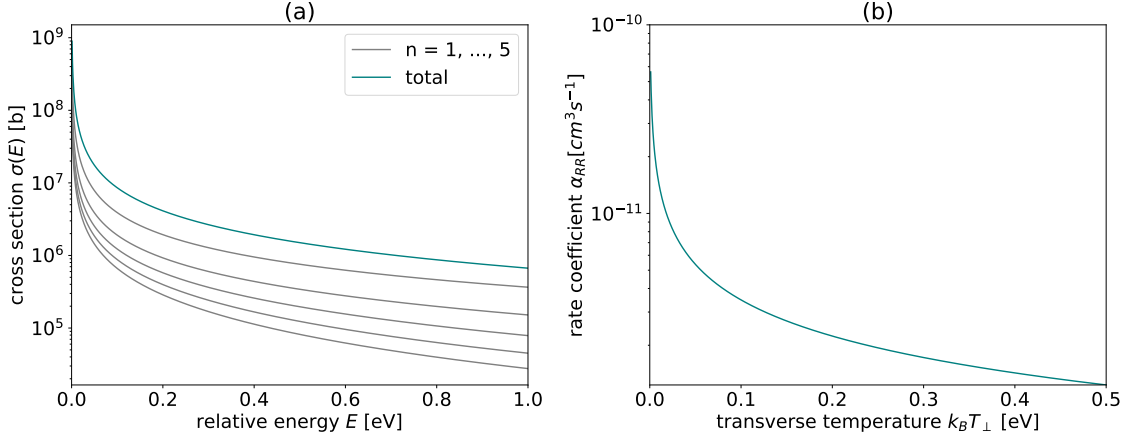
Figure 2.3.: Cross section (a) and rate coefficient (b) of radiative recombination

$$\alpha_{rr} = 3.79(kT_\perp[\text{eV}])^{-0.678}10^{-13}\,\text{cm}^3/\text{s} \qquad \text{(normal)}, \qquad (2.23)$$

$$\alpha_{rr} = 7.88(kT_\perp[\text{eV}])^{-0.645}10^{-13}\,\text{cm}^3/\text{s} \qquad \text{(flattened)}. \qquad (2.24)$$

As one can notice neglecting the longitudinal velocity spread of the electron approximately leads to a doubling of the recombination rate for the same temperature. In case of a finite detectable energy level n_{str} a good approximation was already derived by W. Schwab [34]:

$$\alpha_{rr} = 2\pi^2 r_e c \lambda_e \frac{2R}{\sqrt{m_e c^2}} \frac{\sqrt{\pi}}{\sqrt{kT_\perp}} \sum_{n=1}^{n_{str}} \frac{1}{n}. \qquad (2.25)$$

In order to obtain an analytical solution he solved the problem in the limit of low energies compared to the Rydberg energy for which $\sigma_n(E) \sim 1/(nE)$.

Nevertheless both solutions show an inverse proportional behaviour of the recombination coefficient with respect to the transverse electron temperature. This simply resamples the inverse proportionality of the cross-section from the relative energy between electron and ion. The lower the relative energy between electron and ion (expressed in a higher transverse temperature), the more likely are both to recombine into a bound state. This key message helps to interpret the development of the recombination rate during the electron cooling cycle.

2.3.2. Field Ionization

As mentioned before electrons recombining into higher excited states may be field ionized by motional electric fields, if their binding energy not high enough [30]. Since the population probability for low electron energies of a certain Rydberg-level scales with $1/n$ (see equation 2.17) this effect has a rather small influence on the recombination coefficient but should be discussed here for the sake of completeness.
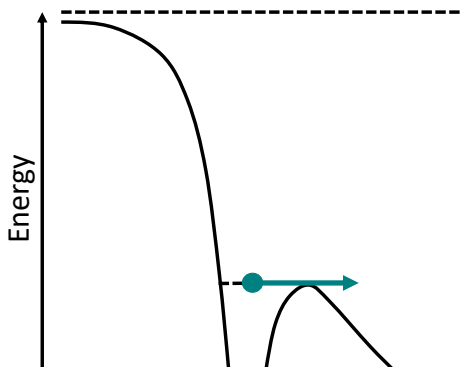
Figure 2.4.: Schematic representation of barrier suppression ionization

Particles moving through a magnetic field are exposed by a motional electric field $\vec{E}_{mot}$. With the knowledge of the magnetic field $\vec{B}$ the induced motional electric field can be obtained by means of the *Lorentz transformation*:

$$\vec{E}_{mot} = \vec{v} \times \vec{B}. \tag{2.26}$$

The motional electric field modifies the Coulomb potential of the nucleus by a homogeneous, linear term introducing a asymmetry. While the nucleus potential increases to one site, it decreases to the other side (see figure 2.4):

$$V(r) = -\frac{Ze^2}{4\pi\epsilon_0 r} - eE_{mot}r. \tag{2.27}$$

r represents the distance of the electron to the nucleus and ϵ_0 the vacuum permittivity. In the following one can use the semiclassical *Barrier Suppression Ionization Model* (BSI) to find a formula for the energy threshold of the electron in the atomic potential to be field ionized E_{str}. This means, electrons captured into higher levels with a binding energy below the energy threshold $E_n < E_{str}$ are stripped of by the motional electric field and the ions returns back to the original beam or get lost. Apart from that electrons whose binding energy exceeds the energy threshold $E_n > E_{str}$ in the semiclassical picture will not get stripped.

For a more precise description one in theory could include tunneling ionization into the current discussion, because electrons in lower excited levels with a binding energy

above the energy threshold can escape from the potential of the nucleus via barrier tunneling. Anyway, for the depth of detail of the current discussion it is not of relevance. Since in the BSI Model only over-the-barrier ionization plays a role, one can calculate the local maximum of the modified atomic potential $dV_{max}/dr = 0$ to find an expression for the energy threshold:

$$E_{str} = -4m_e c^2 \sqrt{\frac{Z\beta B_\perp \alpha \mu_B}{m_e c^2}}, \qquad (2.28)$$

where $\mu_B = e\hbar/2m_e$ denotes the Bohr magneton. Since only the magnetic field component perpendicular to the beam $B_\perp$ contributes to the motional electric field it was made use of $E_{mot} = \beta c B_\perp$ at this point. The respective energy level n_{str} is given by comparison with the binding energy of an energy level:

$$E_n = -\frac{R}{n^2}. \qquad (2.29)$$

Electrons captured in a energy level $n \le n_{str}$ remain bounded, while electrons in higher excited states $n > n_{str}$ will be stripped off by the motional electric field. One obtains

$$n_{str} = \left\lceil \frac{1}{2} \sqrt[4]{\frac{R^2}{Z\beta B_\perp \alpha \mu_B m_e c^2}} \right\rceil = \left\lceil 2.706 \sqrt[4]{\frac{1}{Z\beta B_\perp[T]}} \right\rceil, \qquad (2.30)$$

where $\lceil \cdot \rceil$ represents the ceiling function mapping a real number to the least integer that is greater than or equal to its own. After cooling the recombined beam is travelling through different sections of magnets starting with the toroid magnet of the electron cooler that separates the electron beam from the ion beam and guides it to the collector. An approximation of the perpendicular magnetic field B_{tor} experienced by the recombined particles can be derived from simple geometric considerations. Nevertheless measurements have shown that these approximations are in good agreements with the actual field (see section A.1). The maximal perpendicular field in the toroid section is having the form:

$$B_{tor} = \mu_0 \frac{N_{tor} I_{tor}}{4\pi r_0} \frac{360}{\phi} = \frac{B_{guid}}{2}. \qquad (2.31)$$

Here N_{tor} and I_{tor} are the number of coil windings and the current applied to the toroid, ϕ the angle of the toroid magnet and r_0 the radius with which the particles are entering the toroid magnet. By applying equation 2.31 to equation 2.30 one is able to find the minimum excitation level for a recombined electron-ion-pair to be field ionized by the toroid field:

$$n_{tor} = \left\lceil 3.218 \sqrt[4]{\frac{1}{Z\beta B_{guid}[T]}} \right\rceil. \qquad (2.32)$$

The energy dependence of the stripping energy E_{tor} and level n_{tor} calculated for proton and deuteron beams ($Z = 1, 2$) is shown in figure 2.5. It was assumed that
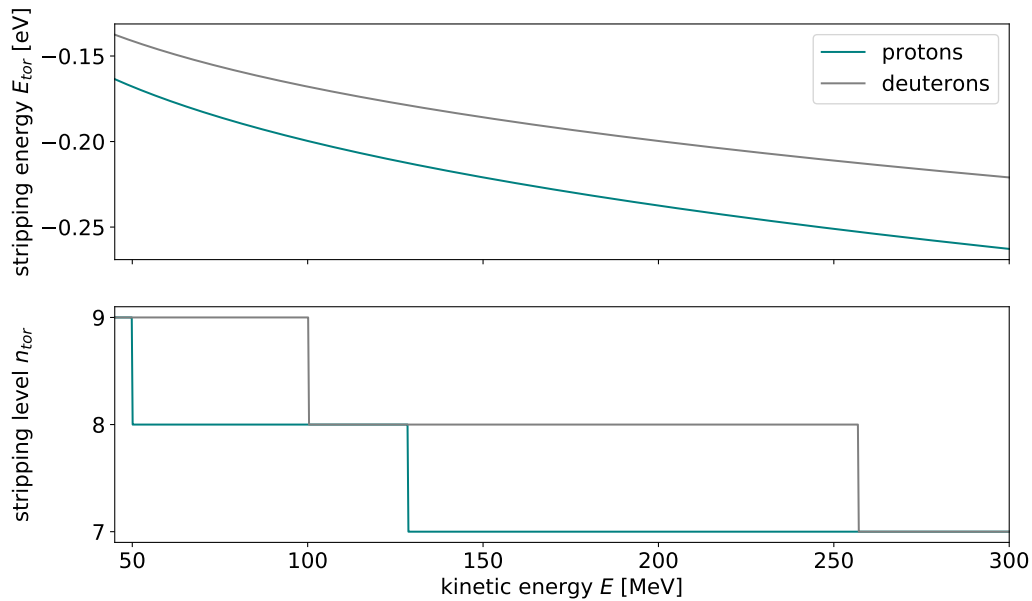
Figure 2.5.: Kinetic energy dependence of the stripping level n_{tor} and stripping energy E_{tor} in the electron cooler toroids

the recombined particles are passing the toroids at the center. Furthermore a guiding magnetic field of B_{guid} = 50 mT was considered.

At injection energy, which is 45 MeV for protons and 78 MeV for deuterons, all levels above the ninth energy level get stripped, while for higher kinetic energies the stripping level decreases down to seven.

After leaving the electron cooler the recombined beam is passing through a series of steerer magnets. The motional electric field of the steerer magnets can be neglected for the current discussion, because the transverse component in the magnetic field is much lower than the one of the cooler toroids. Incidentally, on the way to the bending dipoles higher excited states can already de-excite by radiative transitions. When passing the first magnetic dipole at the beginning of the curvature the recombined beam is separated form the remaining ion beam.

The magnetic field of the bending dipoles can simply be calculated from the *beam rigidity*. The beam rigidity describes the effect of a particular magnetic field B_{dip} on the trajectory of a charged particle.

$$B_{dip} = \frac{p}{q\rho} = 3.1\text{T}\frac{\gamma\beta A}{Z\rho[\text{m}]}, \tag{2.33}$$

where p and q is the particles momentum and charge and ρ the bending radius of the storage ring in the curvatures. Using the same concept as above one can find a energy level for electrons to be field ionized by the magnetic field of the dipole magnets:
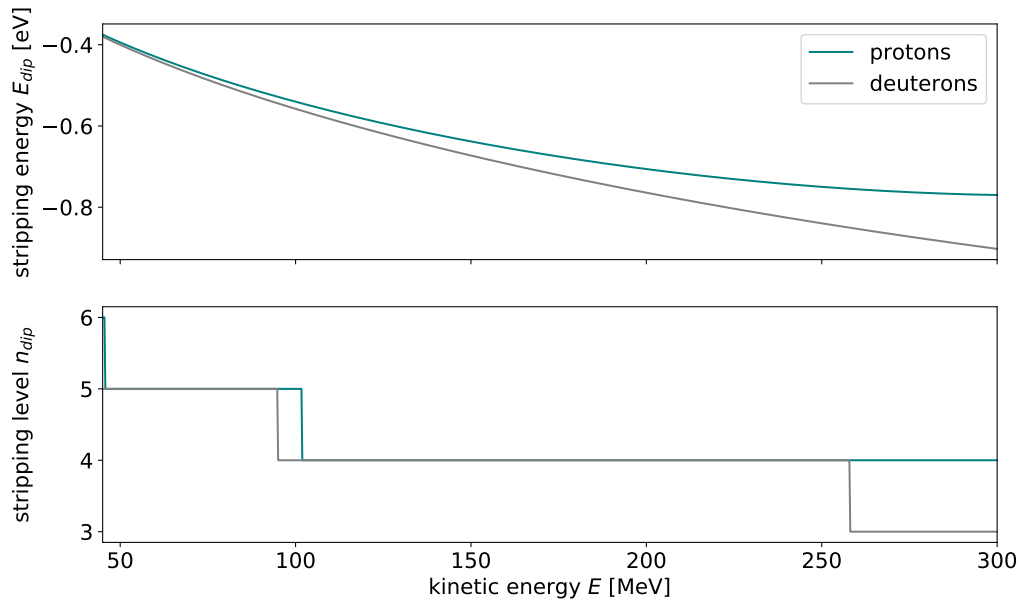
Figure 2.6.: Kinetic energy dependence of the stripping level n_{dip} and stripping energy E_{dip} in the bending dipoles

$$n_{dip} = \left\lceil 2.039 \cdot \sqrt[4]{\frac{\rho[m]}{A\gamma\beta^2}} \right\rceil. \tag{2.34}$$

In figure 2.6 the stripping energy with its corresponding energy level for different kinetic energies of proton and deuteron beams is presented. When cooling at injection in the case of protons all energy levels above the sixth level, whereas in the case of deuterons all levels above the fifth level get stripped. For higher kinetic energies above 100 MeV only levels up to the fourth remain bounded.

3. Neutral Particle Detector

In the this chapter the individual parts of the detection system will be described. In order the reader to get across a better picture of the particle detection the underlying physical processes will be described as well. At this occasion both detector systems, the rate detector as well as the Multiwire Proportional Chambers for beam shape measurements will explained in more detail.

3.1. Overview

Since the trajectory of recombined particles is not bend by magnetic fields anymore they can be decoupled from the storage ring at the first bending dipole after the straight section. The neutral particle detector is installed with a distance of $24.3\,\mathrm{m}$ to the center of the cooling section of the 100 keV-Cooler.
A schematic representation of the neutral particle extraction line is shown in figure 3.1.
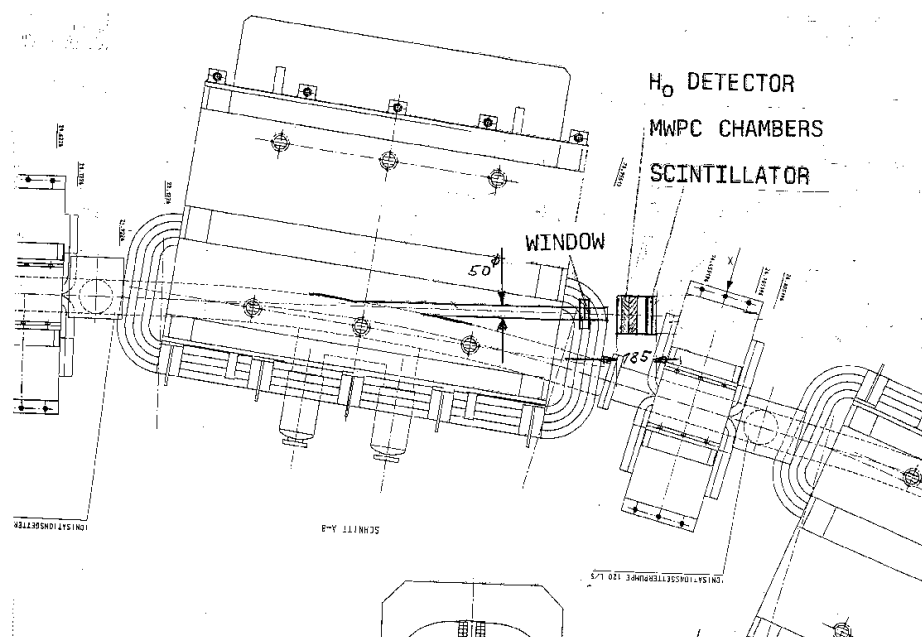
Figure 3.1.: Extraction line for recombined particles [21]

Neutral particles are extracted through $50\,\mathrm{mm}$ broad and $750\,\mathrm{mm}$ long tube ending with a $50\,\mu\mathrm{m}$ thin extraction window. When passing through the extraction window

18

electrons get stripped from the neutral particle leaving the positive charged ion that can in the following be detected in the neutral particle detector. Firstly, the neutral particle detector consists of two Multiwire Proportional Chambers (MWPC) turned by an angle of 90° for horizontal as well as vertical profile measurement. Secondly, two plastic scintillator paddles are positioned to count the absolute rate of recombined particles.
The following section will enlarge upon both detector types in more detail.

3.2. Multiwire Proportional Chambers

The MWPC in its functionality is comparable to a proportional counter used in Geiger-Müller counter. It consists of a thin chamber filled with gas in which an array of parallel wires is installed. The wires are connected to an high voltage (anode). The conductive walls of the MWPC are grounded. The MWPCs at COSY are using 64 thin wires having a distance of 1 mm from each other. As ionization gas a gas mixture of argon and isobutane is utilized.
A particle passing through the chamber will ionize the gas along its trajectory. The resulting ions and electrons are accelerated by the electric field across the chamber, causing a localised cascade of ionization (Townsend avalanche). This will lead to a current flowing from the wire closest to particle trajectory to the walls of the wire chambers. At each of the wires current pulses can be detected separately in order to generate the beam profile. A systematic presentation of such a wire chamber is shown in figure 3.2. Since the particles will just slightly be decelerated within the MWPC a parallel operation with the rate detector is possible.
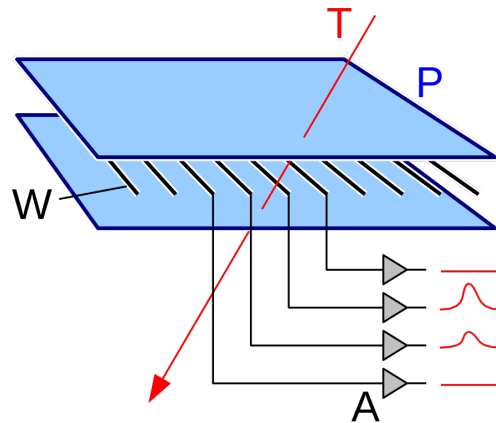
Figure 3.2.: Functional principle of MWPCs [17]

3.3. Rate Detector

After the particles have passed the MWPCs they will be decelerated and detected within the rate detector, to determine the rate of neutral particles generated during the cooling process. The rate detector consists out of two plastic scintillators, each having a thickness of 5 mm. Everytime a particle passes trough both scintillators parallel current pulses are generated. By counting the coincidence of the signals the rate of recombined particles can be determined. A more detailed description is given in the following chapter.

3.3.1. Scintillator Paddles

In general scintillators can be made from anorganic as well as from organic materials, where in the latter case the scintillation material can be available in the crystalline, fluid or polymeric form. Depending on the material (anorganic/organic) different mechanisms are responsible for the scintillation effect.
The scintillator material of choice is the plastic scintillator *NE102A*. Thus only the effect of organic scintillation will be discussed further at this point. The properties of the scintillation material *NE102A* are given in table 3.1. Its density is close to water, however the refractive index is much greater than that of air. Therefore total internal reflection is possible on the surface of the scintillator.
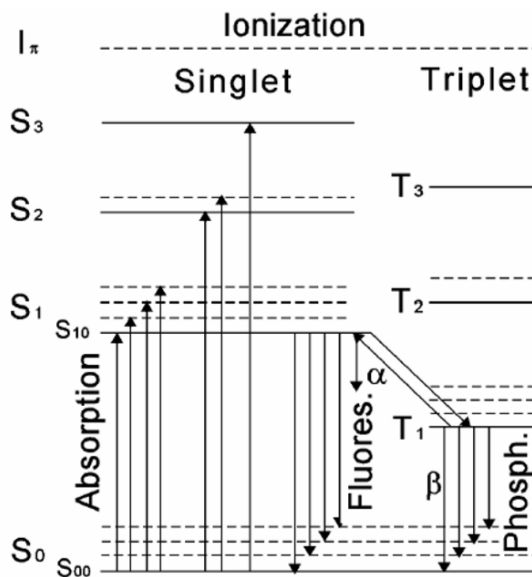
Figure 3.3.: Exemplary energy levels of organic molecules [24]

When a particle passes trough the scintillator, energy from the particle is absorbed by the molecules and electrons are excited from the ground state S_0 in a into excited states S_1, S_2, S_3 and further. For organic molecules the energetic distance between the ground state S_0 and the first excited state S_1 is on the order of several eV, while the

NE102A	
Density	$1.032\,\text{g/cm}^3$
Refractive index	1.581
Light output	65 %
Decay time	2.4 ns
Emitted wavelength	423 nm

Table 3.1.: Physical properties of the plastic scintillator *NE102A* [25]

distance between the excited states is much smaller. Each level can furthermore be subdivided into different vibrational states denoted by the second subscript. Electrons that were excited into higher excited states like S_2 and S_3 and higher vibrational states like S_{11} and S_{12} quickly de-excite into the first excited state without the emission of radiation. This process is known as *internal degradation*. After a short time a population of excited molecules in the state S_{10} is produced.

The scintillation light is now is emitted through the transition of excited electrons from S_{10} back to the ground state S_{00}. The effect is called *flourescence*. Organic scintillators offer extremely fast light pulses with a decay time of just a few nanoseconds. The best mathematical description the light pulses in organic scintillators appears to be the product of a Gaussian and an exponential function [25]:

$$N(t) = N_0 f(\sigma, t) \exp\left(\frac{-t}{\tau}\right), \tag{3.1}$$

where $f(\sigma, t)$ denotes the Gaussian function with a standard deviation σ and τ the decay time. For the description of light pulses in *NE102A* $\sigma = 0.7\,\text{ns}$ and $\tau = 2.4\,\text{ns}$ can be used. Since the light produced by fluorescence emission has a lower energy than the one required for absorption (except S_{00} to S_{10}), the overlap between the emission and absorption spectra is small. Therefore most of the scintillation light can pass through the scintillation material without being absorbed.

Triplet states like T_0 can de-excitate via a related process. However, the transition from T_0 to S_0 is highly forbidden by multipole selection rules. Therefore processes of *Phosphorescence* decays slowly leading to delayed light pulses. The contribution to the total light output in the most scintillation materials is extremely low.

3.3.2. Photomultiplier

The scintillation light will be guided to a photomultiplier tube (PMT). A PMT is an extremly sensitive vacuum tube with whose help a weak light signal is converted into a measurable current flow. A drawing of a typical PMT can be seen in figure 3.4. It mainly consist out of a photocathode, several dynodes and an anode housed in an evacuated glas tube.

Incoming photons will hit the photocathode located at at entry-window of the vacuum tube. Due to the photoelectric effect primary electrons are released from the
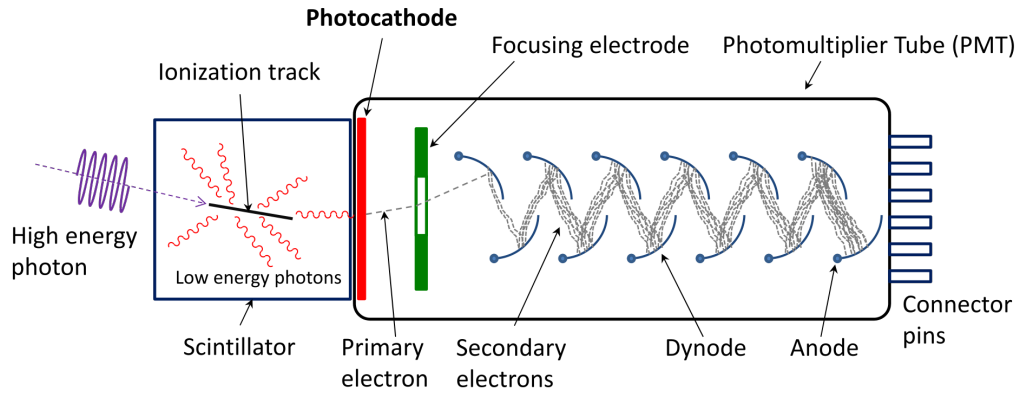
Figure 3.4.: Functional principle of PMTs [16]

surface of the photocathode, which typically consists of vapor-deposited metal. The primary electrons will be accelerated by a focussing electrode towards the electron multiplier.

The electron multiplier is build up from multiple dynodes, where each of the dynodes is set to more positive potential than the previous one. The primary electrons move towards the first dynode. When striking the surface of the dynode several more electrons are emitted as a consequence of the effect of secondary emission. These low energy secondary electrons are afterwards accelerated towards the second dynode, which is held on a more positive potential, where even more electrons will be emitted. Due to the cascade effect the number of electrons will increase exponentially, before they encounter the final cathode. Assuming k being the number of secondary that is emitted per incoming primary electron at each dynode and n being the number of built-in dynodes, one can estimate the number of electrons reaching the cathode to be on the order of k^n [25].

The electron detected in the cathode will lead to a negative current pulse, that than can be processed futher by the analog-to-digital converter, as it is described in the next chapter.

3.3.3. High Voltage Supply

The PMT is connected to a *CAEN SY5527LC* power supply with an *CAEN AG7435* high voltage module [10] [9]. It offers an output voltage between $0 - 3.5\,\mathrm{kV}$ for each of the PMTs. The power supply comes with ethernet communication and is integrated into the EPICS control system. This allows an automated control via the control system.

In order to distinguish the background signal from the signals caused by the neutral particle beam the high voltage has to be calibrated to the be set right. The calibration was done with the help of a radioactive source. A short description of the high voltage calibration can be found in section A.2.

4. Realization of the Data Acquisition System

After introducing the detector system, the data acquisition system (DAQ) shall be discussed in more detail. In the following a short introduction into field programmable gate arrays (FPGA) with its electronic structure and its corresponding design flow will be given as well as an overview of the used technologies. Lastly the implementation of the data acquisition and the monitoring system will be described further.

4.1. Introduction into FPGA technology

Field programmable gate arrays are integrated circuits that are designed to be configured by the user itself after manufacturing for a specific application. The term "field programmable" refers to the ability to customize the functionality of the device "in the field", while the term "gate array" is related to the basic internal architecture that makes the reconfiguration of the device possible. FPGAs come along with large number of logic gates. These logic gates can be rewired as many times as required to carry out a certain task.

FPGAs offer the best trade-off between processors (CPU) and application-specific integrated circuit (ASIC) in terms of customizability and computation efficiency.

CPUs are general purpose chips and thus can perform any function based on the program that is uploaded to them. The internal hardware structure of a CPU is defined by the vendor and can not be modified. In a CPU a specified set of instructions is executed in a sequential manner by arithmetic logic units (ALU). While CPUs are optimal for single process systems where code needs to be executed in a sequential or linear manner, they are highly limited in the parallelization of processes by their number of cores.

ASICs on the other hand are designed for one specific purpose. They perform with low power consumption at the highest possible computational speed, since all processes can be synchronized and parallelized best possible. In ASICs the utilized circuit is permanently drawn into silicon, what makes them not reprogrammable after production. Unfortunately they require significantly higher development costs making them only favourable for mass production.

Due to their highly parallel nature and ability to implement custom algorithms, FPGAs are very beneficial to be used in digital signal processing applications such as the signal processing of particle detector pulses. Due to the high demand of computational acceleration FPGAs nowadays can be found in many different areas.

At COSY fast processing and integration of detector data is needed at many different places outside the neutral particle detection. That is why FPGAs are also used in many other application such as the Beam Loss Monitoring or the Ionization Profile Monitoring.

4.1.1. Electronic Architecture

The basic structure of an FPGA can be seen in figure 4.1. A FPGA mainly consist of configurable logic blocks (CLB), input/output blocks (IOB) and programmable switch blocks (PSB) interconnected via wire lanes.

A single CLB can be configured to execute any logic or sequential operation. The core of a CLB consists of one or more look-up tables (LUT). Such a LUT is able to store a predefined output for every single combination of inputs. Modern FPGAs currently use LUTs with six independent inputs. LUTs offer a fast way to retrieve the output for a certain logic operation since possible results are already stored and then referenced rather than calculated. Besides LUTs CLBs normally also contain additional components like multiplexers and flip-flops.

When linked together CLBs are able to execute any arithmetic or logic function. The connection between different CLBs is established with the help of PSBs. Looking at figure 4.1 a PSB is placed whenever a vertical and a horizontal wire intersect. This allows every two CLB to be connected with each other. In this architecture, when a wire enters a switch box, there are three programmable switches that allow it to connect to three other wires in adjacent channel segments.

Finally IOBs allow the FPGA to communicate with other devices [40].
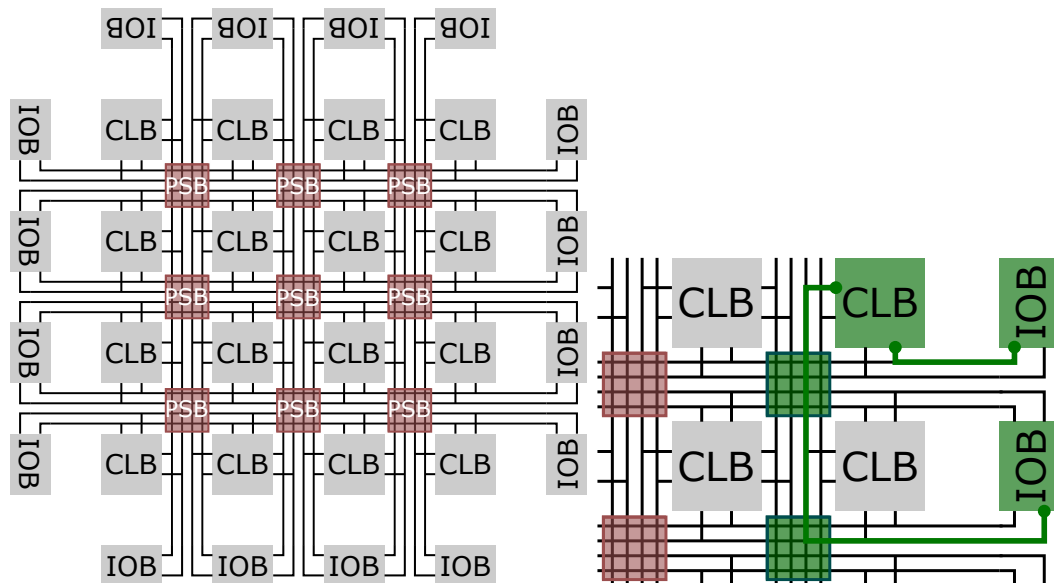
Figure 4.1.: Exemplary architecture and signal routing on a FPGA

4.1.2. Design Flow

With FPGAs, the benefits of high performance and reconfigurability come with the costs of added complexity, when implementing functions to the device. In FPGA design one challenge that engineers face is the need to work with both hardware as well as software components, where each of them has its own difficulties. Following, when facing a FPGA design one must go through different step between the design idea and the implementation on the hardware. Those steps are usually referred to as *design flow.*

Starting from the design idea like in software programming one needs to transform the idea into some kind of computerreadable representation. This is normally done with the help of hardware description languages (HDL) - as they are also used in the design of ASICs - such as *Verilog* or *VHDL* [45] [46]. HDLs differ from software programming languages in the sense that they do not support the concept of sequential execution of statements in the code.

Although it is not strictly necessary to achieve a successfully compiled load file the HDL code should be simulated in order to prove if the code delivers the desired functionality. For this purpose many different simulation programs are available. In this work the simulator of the *Vivado Design Suite* was used.

In the following the HDL code gets synthesised meaning it is translated into operating logic. The synthesis can be thought of as a bridge between the human readable HDL code and a gate-level representation. Synthesis tools are provided by the vendor of the FPGA chip.

The last step one needs to take care of the placing and routing. The placer takes the synthesized netlist and chooses a place for each of the primitive cells inside the chip. The router's task is then to interconnect all these primitive cells together satisfying the timing constraints of the utilized FPGA. The most obvious constraint for a design is the frequency of the system clock, but there are more involved constraints one can impose.

After successful completion of the former steps a load file (also called bitstream) is generated containing the configuration that can be loaded into the FPGA. The bitstream is typically loaded on some volatile configuration memory that is distributed over the chip [35].

4.2. EPICS

The *Experimental Physics and Industrial Control System* is an open source software environment used for the development of distributed control systems for large experiments such as particle accelerators, telescopes and fusion reactors [18]. Those types of experiments contain many points where data is recorded and needs to be transferred to many different places for operational as well as for analytical purpose. Originally developed jointly by the Los Alamos National Laboratory and the Argonne National Laboratory, it is nowadays used and developed further by many facilities throughout

the world.

EPICS uses Client/Server and Publish/Subscribe techniques to communicate between the various computers. Meaning servers, which are called Input/Output Controllers (IOC) perform real-world I/O and local control tasks, and publish this information to clients using the Channel Access (CA) network protocol. The CA protocol is specially designed for high bandwidth and real-time network applications that EPICS is used for, and is the reason why it can be used to build a control system comprising hundreds of computers.

The data itself is exchanged via an special type of data structure the so called *Process Variable* (PV). One can imagine a PV as an complex data structure which contains next to the main information as the name and the value of a measured variable further information such as the unit and the time stamp of a measurement. A PV can also carry more complex measurements as waveforms or machine states or can be used for the processing of other PVs. The exact structure of a PV can be defined by the user itself through a database in form of a database record. An exemplary database record of a PV is shown below:

```
record(calc,"RATE"){
   field(DESC  , "Positive-Edge Rate")
   field(EGU   , "Hz")
   field(CALC  , "A/B*C")
   field(INPA  , "CNT:DIFF")
   field(INPB  , "CLK:DIFF")
   field(INPC  , "CLK:FREQ")
}
```

Listing 4.1: Exemplary Epics PV

The shown PV takes the other PVs `CNT:DIFF`, `CLK:DIFF` and `CLK:FREQ` as the inputs *A*, *B* and *C* and performs the calculation $AB^{-1}C$ on them. The information later is published under the PV-name `RATE`. Further information like the unit and a description of the PVs are stored within the EGU- and DESC-fields.

In addition, with the EPICS Archiver Appliance (Archiver) EPICS offers a possibility to permanent archive acquired data [4]. This allows next to real-time analysis of the data a simple backtracking of the measurement as well.

4.3. Red Pitaya STEMlab board

The Red Pitaya STEMLab (STEMLab) is an open-source software instrumentation platform capable of different measurement tasks. The development board itself is distributed by the Red Pitaya company, while the source code is available online as open-source [33]. The public access to the source code makes the STEMLab highly customizable and therefore suitable for various tasks.

The core of the STEMLab is the *Xilinx Zynq 7010 System-on-Chip* (SoC) device. In a SoC all electronic parts are integrated within one single chip. It contains an *ARM Cortex-A9 CPU* as well as an *Xilinx Zynq 7010* FPGA. The ARM CPU is capable to

RF Input	
Sample rate	$125\,\text{MS/s}$
ADC resolution	10 bit
Input impedance	$1\,\text{MOhm}/10\,\text{pF}$
Full scale voltage range	±1 V (LV) and ±20 V (HV)
Absolute max. Input	$30\,\text{V}$
Overload protection	Protection diodes

Table 4.1.: Specification of the STEMlab RF inputs [31]

run a Linux Operating System, that must be installed on an external SD-Card. The SD-Card can be plugged into the integrated SD-Card-Reader. The most important specifications of the STEMLab can be found in table 4.2.

Figure 4.2.: Hadware overview of the Red Pitaya STEMlab board

Besides the SoC the STEMLab is equipped with two independent Analog-to-Digital-Converter (ADC) and Digital-to-Analog-Converters (DAC). Each operates with a sampling rate of $125\,\text{MS/s}$, while offering a resolution of 14 bit [32]. The specifications of the ADCs are given in table 4.1.

In addition the STEMLab features two extension connectors. One extension connector provides 16 digital IOs of which one can be used as an external trigger for data acquisition. The second extension connector offers pins for different communication protocols like I2C, UART and SPI, as well as the possibility to connect the development board with an external ADC clock and 4 further analog outputs and inputs running at a lower sampling rate of $100\,\text{kS/s}$ with a 12 bit resolution. The network connection of the STEMLab is guaranteed via Ethernet (see figure 4.2).

Hardware Overview	
CPU	DUAL CORE ARM CORTEX A9
FPGA	FPGA Xilinx Zynq 7010
RAM	512 MB
System Memory	Micro SD up to 32 GB
Power Connection	Micro USB
Power Consumption	5 V, 2 A max.

Table 4.2.: STEMLab 125-14 Specifications [31]

4.4. Implementation

When particles pass the plastic scintillators, they produce light, which is then converted to an analogue electrical signal in the photomultiplier tubes. Electric pulses afterwords are digitized by the two fast analog-to-digital converter of the Red Pitaya development board. The digitized pulses are further processed on the FPGA. The FPGA provides the collected counts to the IOC, which calculates the rate of detected particles and publishes the acquired data to the EPICS control system (see figure 4.3).
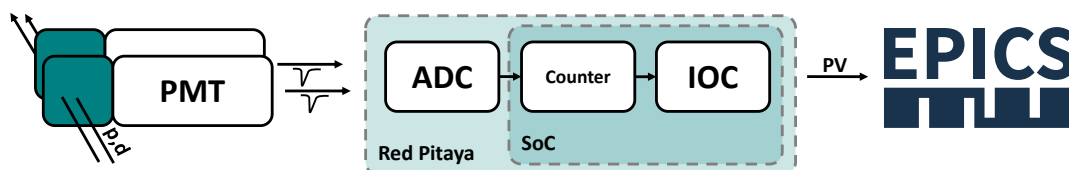
Figure 4.3.: Signal flow scheme of the neutral particle detector

4.4.1. Analog-to-Digital Conversion

ADCs are electric circuits that convert an analog signal to its corresponding digital code. The conversion of the analog input voltage into its digital code can be done with the help of a transfer function. In an ideal ADC the transfer function is a linear function given by the following formula:

$$C_{out} = \frac{2^n}{V_{fsr}} \cdot V_{in},\tag{4.1}$$

where n is the resolution of the ADC, V_{in} the input voltage and V_{fsr} the full scale range. The full scale range is given by $V_{fsr} = V_{hi} - V_{low}$, where V_{hi} and V_{low} are the upper and lower extremes of the voltages, that can be processed by the ADC.

On the STEMlab the voltage scale for each of the ADCs is set by input jumpers. With the help of the input jumpers the voltage range can be adjusted to either ±1 V or ±20 V. In this work a voltage range of ±1 V was chosen, because the incoming pulses are on the scale of several mV.

The calibration was carried out with the help of a voltage generator. At five defined voltages (−1 V, −0.5 V, 0 V, +0.5 V, +1 V) several measurements of the ADC output where taken. From the fit of the ADC samples a linear function can be fitted with whose help the three calibration coefficients can be determined.

The calibration coefficients are stored in EEPROM (electrically erasable programmable read-only memory) placed on the development board. An EEPROM is a non-volatile type of memory. Therefore the calibration coefficients will not change when turning off the development board.

4.4.2. Signal Processing

After the digitisation of the two detector signals the digital signals will be processed further on the FPGA. In figure 4.4 a data flow chart listing all important signal processing blocks that were implemented on the FPGA is shown. The FPGA firmware has been developed using the Verilog HDL and the Vivado Design Suite.
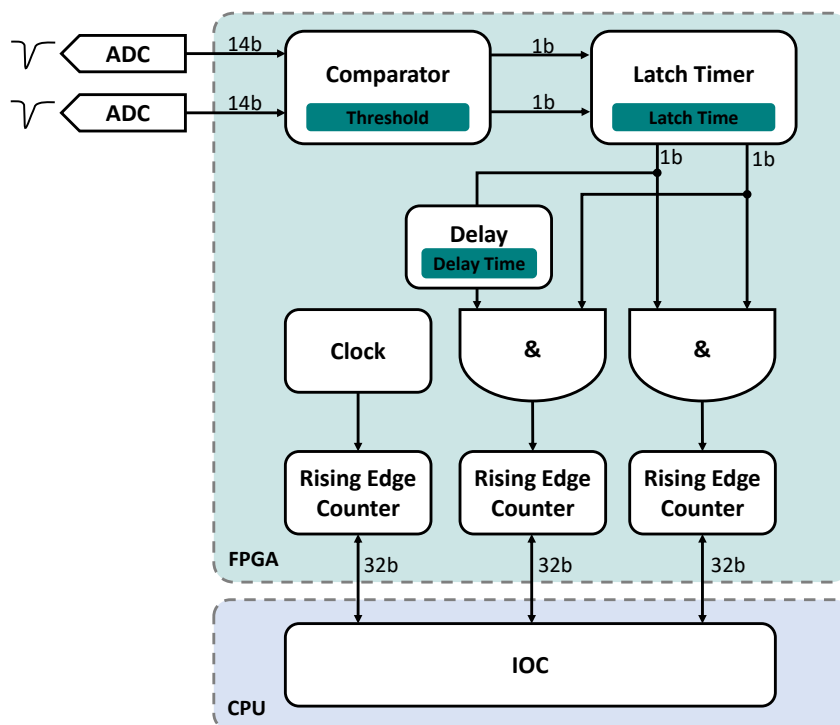
Figure 4.4.: Implemented signal flow on the FPGA

Comparator. At the beginning each of the two digitized signals is processed in a *digital magnitude comparator*. The function of this block is to receive data from the ADCs and to detect the pulse signals. The comparator compares the incoming pulse signals with a constant threshold value to detect an incoming pulse. The threshold value is stored in a register in form of a 14-bit number. In this application the threshold for the signals is set to a value of $-15\,\text{mV}$ and $-25\,\text{mV}$. At each clock cycle a comparison between the ADC signal and the threshold value takes place. If the input signal is lower than or equal to the threshold value the output of the comparator is set to logic 1. If the input signal is greater than the threshold value the output of the comparator equals logic 0.

Latchtimer. Afterwords each of the two 1-bit outputs of the comparator is then fed into a latchtimer. The purpose of the latchtimer is to keep the detected pulses at a fixed length. The latchtimer takes the comparator output and a latchtime as the inputs. The latchtime has the size of 8-bit is as well stored in a register as the threshold value of the comparator. The registers can be accessed by the IOC and can therefore be changed via EPICS. The latchtime determines the length of the latched pulse in number of clock cycles. Since one clock cycle is of the length of 8 ns, it allows to vary the length of the latched pulses between 16 ns and $2\,\mu\text{s}$.

The latchtime also defines the deadtime of the system. The latchtimer works in a nonparalyzable manner, meaning the system is not affected by events that occur within its deadtime (latchtime). Let τ be the latchtime of the system. If the latchtimer is triggered by a detected pulse, the system is blind for further pulses that occur within the time τ after the detection. If R_m is the measured rate, the fraction of time for which the system is dead is $R_m\tau$. The number of pulses that can not be detected $\Delta R = R_n - R_m$, where R_n denotes the true rate, can be estimated by the equation [43]:

$$\Delta R = R_n - R_m = \frac{R_m^2 \tau}{1 - R_m \tau}. \tag{4.2}$$

A latchtime of 48 ns seconds was chosen, which corresponds to the duration of 6 clock cycles and is the closest to the length of the analog pulses by the PMTs. If one assumes a pulse rate of 5000 per second the number of non-detected pulses caused by the deadtime of the system amounts 1 pulse per second, what corresponds to a loss below $0.1\,\%$.

The latchtimer operates in a sequential manner, meaning at each clock cycle the output of the former clock cycle is required. As mentioned before HDLs do not support the concept of sequential execution of statements. For this purpose, one has to make use of finite-state machines (FSM), or more precise a *Moore Machine.* A FSM is an abstract machine, that can be in one or a finite number of states at a given time. The current state of a FSM can change from one to the other in response to an external input. A Moore Machine is a state machine, whose output values just depend on his current state [12].

In this implementation a Moore Machine with exactly two states was chosen, the ON-

and the OFF-state. As one might expect, in ON-state the output of the latchtimer equal to logic 1, while in the OFF-state the output is equal to logic 0. The module is waiting for a rising edge of the comparator output - meaning a pulse is detected - for a transition from the OFF-state into the ON-state. At the transition into the ON-state a timer will be set to the given latchtime. With each clock cycle the timer will now decrease by one. When the timer reaches 0 the state will be reset into OFF-state. Furthermore the latchtimer can be reset at any time. A state diagram of the implemented Moore Machine can be found in figure 4.5.
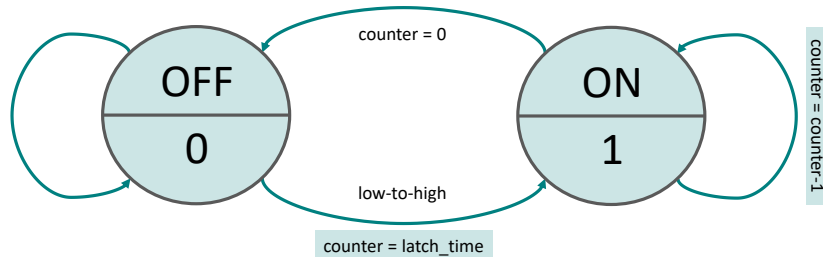
Figure 4.5.: Moore Machine of the implemented latchtimer

In the following both outputs of the two latchtimer are brought into coincidence via an AND-gate. Besides, one of the latched signals will be taken and delayed for a certain number of clock cycles. By bringing the delay signal in coincidence with the other undelayed signal, the frequency of random coincidences, will be determined. For a detector with two scintillator paddles the random coincidence rate R_{rand} is given by:

$$R_{rand} = 2R_a R_b \tau, \tag{4.3}$$

where R_a and R_b represent the pulse rate delivered by each of the paddles and τ the latchtime. It is obvious that in order to minimize the rate of random coincidences one simply needs to decrease the latchtime τ. Nevertheless, the coincidence of both of the latched pulses needs to be larger than 1 clock cycle in order to trigger the counter. Assuming a pulse rate of 5000 per second delivered by each of the paddles the detector has a random coincidence rate of 2 pulses per second and therefore has a vanishing influence on the total coincidence rate.

Delay. The clocked delay has been implemented in form of a shift register. Shift registers consists of cascading flip-flops/registers in a chain, where the output of one register is connected to the input of the next one. The number of registers in the chain dictates how many clock cycles it will take an input value to propagate to the output of the chain and therefore sets the delay time in clock cycles.

Count taking scheme. Each time the coincidence signal changes from logic 0 to logic 1 a counter is triggered to increments its current value by one. Next to the coincidence signal each signal will be counted independently. All signals are counted with a depth of 32-bit.

In order to determine the rate of the coincidence signal, one has to take the derivative of its count. This is done by making use of the *two-point backward finite difference formula*:

$$\frac{df(t_n)}{dt} = \frac{f(t_n) - f(t_{n-1})}{t_n - t_{n-1}}, \tag{4.4}$$

where the derivative of a function f at a certain time step t_n just depends on the value of the function at the previous time step t_{n-1} and the current time step t_n and the past time between both time steps. For this purpose an other counter is introduced counting the number of clock cycles. Additionally a slower clock with a frequency of $10\,\text{Hz}$ called `clock-keep` is introduced. Such an slower clock can be generated by changing the clock state each time the counted clock is a multiple of $6.25 \cdot 10^6$. At rising edge of `clock-keep` the current value of each counter is written into a additional register. The rate R then can be determined by

$$R = \frac{N_{keep} - N_{curr}}{C_{keep} - C_{curr}} \cdot \frac{1}{8\,\text{ns}}. \tag{4.5}$$

N_{keep} and N_{curr} are the pulse counts written to the keep-register and the one of the current cycle. C_{keep} and C_{curr} are the respective clock counts written to the keep-register and of the current cycle. In order to receive a time resolution one has to multiply the clock counts with the clock period of $8\,\text{ns}$. It is important to mention that the FPGA only provides the pulse and clock count, but does not calculate the final rate. The rate will be determined later by the CPU within the EPICS IOC. This is due to the reason that other than CPUs, working in floating-point arithmetic, FPGAs are working with fixed point arithmetic. Complex calculations underlie larger errors than in floating-point representation while being computationally inefficient compared to CPUs.

4.4.3. Data Acquisition

The ARM processor on the SoC is running a full Linux operating system of only $14\,\text{MB}$, which already contains a SSH server, a nginx server and other tools. Furthermore an EPICS Base of the version 3.15.16 was cross-compiled for the ARM-architecture of the Xilinx SoC and added to the operating system. It provides full channel access and server functionality. In order to communicate with the FPGA via EPICS a custom IOC has to run on the system. In a former project such an IOC has already been developed and has been modified at this point [5]. The IOC provides communication with the FPGA by addressing its registers.

The ARM processor and FPGA are connected via an *Advanced Microcontroller Bus Architectur* (AMBA). AMBA is an open-standard specification for the connection of

the functional blocks on a SoC. Processor and FPGA can communicate via the *Advanced eXtensible Interface* (AXI) protocol. In the AXI protocol the ARM processor is the AXI master and FPGA the AXI slave. The AXI master is able to either write data to a certain register of the AXI slave or to read out the data stored in a certain register by transmitting the memory address that stores the requested data.

A further SoftIOC running on an external server provides additional information about the electron cooler. Bringing all relevant parameters of the electron cooler, COSY and the neutral particle detectors together the SoftIOC is able provide further insights like the transverse electron temperature or the recombination coefficient.

4.5. **Monitoring Web Application**

The tracking of electron cooler parameters such as the recombination rate during the operation is vital. Therefore a real-time monitoring system was implemented to visualize important parameters of the 100 keV-Cooler as well as of the neutral particle detector within one application. Currently at COSY the local application *Control System Studio* (CSS) is used for the implementation as well as for the application of monitoring and operator interfaces [11]. CSS makes the development of graphical user interfaces (GUI) simple, especially because it is delivered with an interface for EPICS Channel Access. Nevertheless to make use of such monitoring systems a former installation of CSS is necessary. This is normally just the case for the computers inside the main control room of the accelerator. In addition CSS requires a royalty-bearing license. Furthermore one may wants to monitor the current state of the electron cooler operation from a location outside the control room.

As it already has been shown by Furukawa *et al.* it is possible to implement monitoring and operator interfaces with EPICS CA in an web application without performance reduction [1]. This has the advantage that the only requirements to access the monitoring system is a stable network connection to the host server and a supported web browser, that has to be installed on the client machine. The latter is dealt with in more detail below. Secondly, the application can be opened independently from the users operating system and therefore also can be accessed from mobile devices like smartphones or tablets.

In order to realize a real-time monitoring system the WebSocket protocol was utilized. The WebSocket protocol first introduced in December 2011 and allows bidirectional communication between a web server and a client [15].

4.5.1. **The Node.js Framework**

For the implementation of the server the *Node.js* (Node) framework together with the *Socket.io* library were used [27][36]. Node is an open-source environment developed to execute JavaScript code outside a web browser and can be used for server side scripting. Node comes with his own package management system simplifying the installation and integration of third party libraries like Socket.io offering a JavaScript implementation of WebSockets.

As an advantage Node works asychronously, which is highly beneficial for single variable updates triggered by EPICS CA. To allow the WebSocket server to access EPICS, one needs to make use of a second JavaScript interface. Such an interface was already developed by R. Clarken within the *Node-Epics* library available for Node [19]. It allows to execute the most basic EPICS functions originally developed in C/C++ such as *caget*, *caput* and *camonitor* within JavaScript.

On the client site the JavaScript library *D3.js* together with standard web technologies like HTML and CSS was utilized to implement a web frontend with real-time data visualization [13]. The D3.js library allows to bind document object model (DOM) elements to data.

34
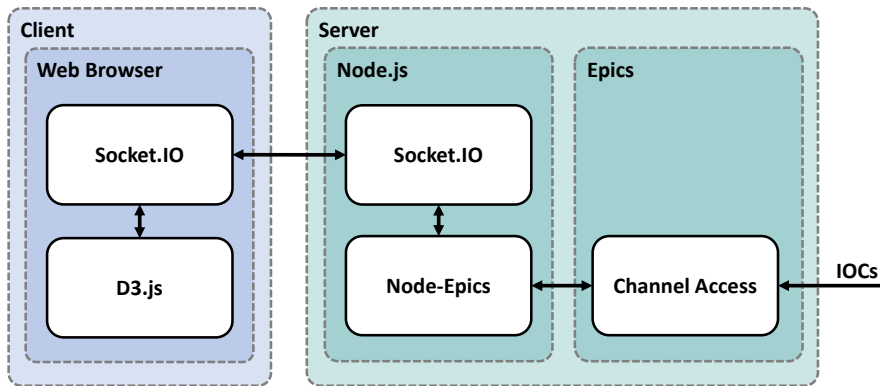
Figure 4.6.: System chart of the monitoring web application

4.5.2. Implementation

A screenshot of the final web application can be seen in figure 4.7. On the left site one can see a sketch of the cooler magnets. Depending on the current magnetic field generated by each of these magnets the respective elements will be colored in a different color as it is shown in the colorbar to the right site of the electron cooler. The most important field strength are also directly shown with their respective value. The line graph further up shows the recombination rate.

On the right site next to the cooler state on the top two tables are shown. The upper table shows the recombination rate again numerically as well as the values of the recombination coefficient and the transverse electron temperature, one can calculate from it. The lower table shows important parameters of the electron beam like the beam current and the beam diameter with expansion factor, that can be calculated from the ratio of the field strength of the gun and cooling solenoid (see subsubsection 2.2.2.1). The upper display indicates if the electron cooler is currently in operation. The whole application is based on one model in format of a json-file. This allows to add PVs used to the monitoring system or to edit them simply without the need to touch the source code. This makes the web application easily maintainable even without programming skills. The signal flow is demonstrated in figure 4.6:

1. The clients web browser sends a handshake request to the server for the Web-Socket connection.

2. After approval the Web Monitor is rendered with the current PV values.

3. On the server site the WebSocket is watching for PV updates via camonitor with the node-epics interface.
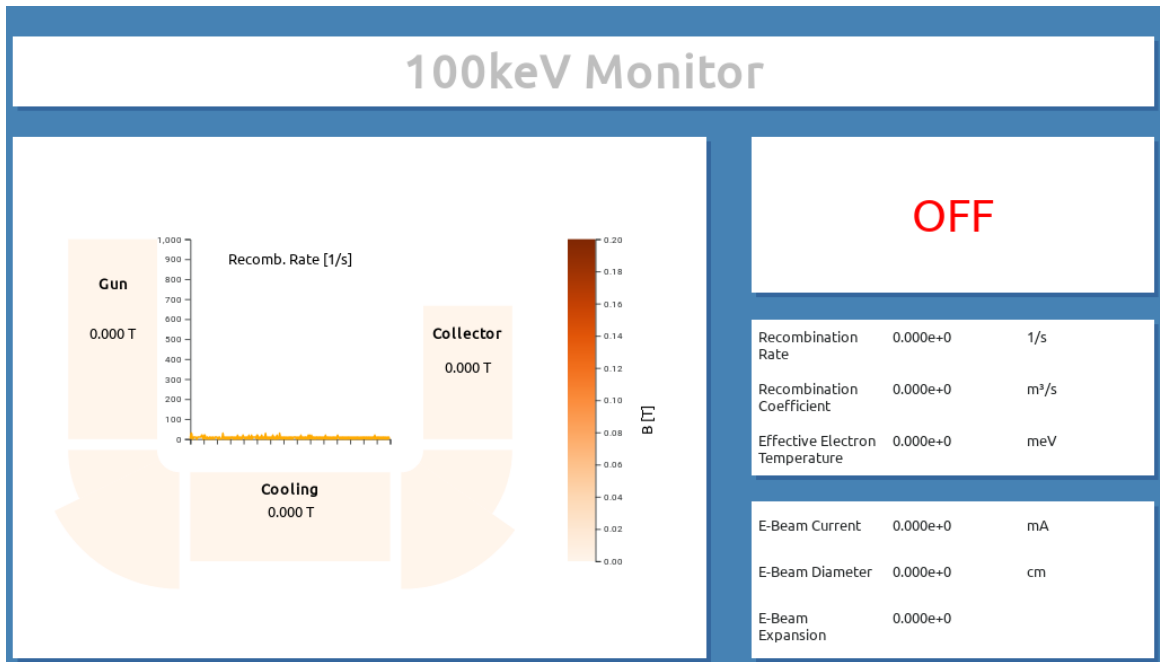
Figure 4.7.: GUI of the monitoring web application

4. Whenever an PV value is updated the new value is send to the client via a WebSocket.

5. The WebSocket on the client side is triggering an update of the DOM element.

The web application has been tested with different browser, in particular *Microsoft Edge*, *Google Chrome*, *Apple Safari* and *Mozilla Firefox*. In addition the application was also tested with multiple clients (<10) without any delay or interruption in the data transmission.
The web application was hosted in a docker container on the thorin server [14], which is connected to the internal COSY network allowing him to connect to EPICS but can also be reached inside the network of the research center. Within the network of the research center the web monitor is accessible in the web browser via the address http://thorin.cce.kfa-juelich.de:49490.

5. Analysis of Recombination Rates

In the following chapter the development of the recombination rate during electron cooling will be discussed in more detail. Furthermore the transverse electron temperature based on measurements of the recombination rate will analysed. The underlying data for this analysis was collected during the JEDI beam time in April and May 2019. A deuteron beam with a kinetic energy of $236\,\mathrm{MeV}$ was studied during this beam time.

5.1. Development of the Recombination Rate during Electron Cooling

In figure 5.1 the time dependency of the total recombination rate R besides the ion beam current I_i and the electron beam current I_e in one exemplary electron cooling cycle is shown.
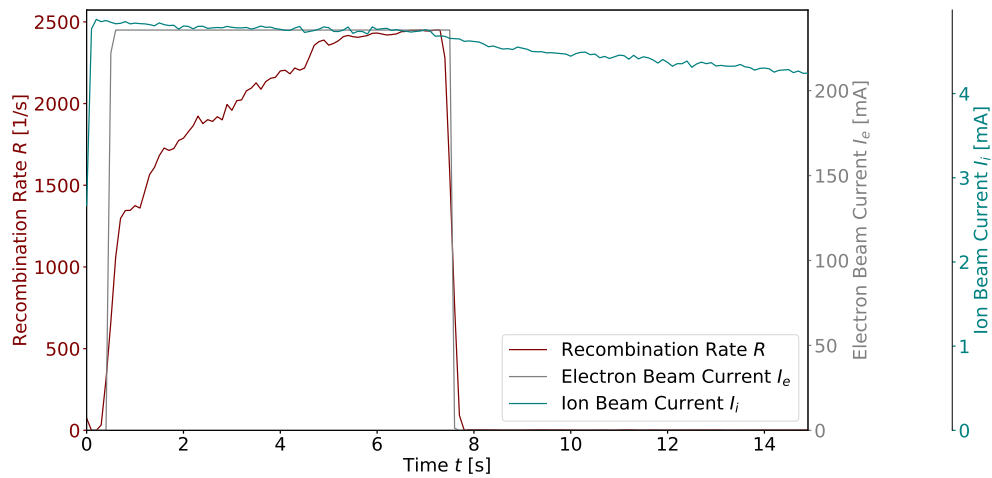
Figure 5.1.: Development of the total recombination rate R, electron and ion beam current I_e and I_i within one electron cooling cycle

At the beginning of the cycle, the deuteron beam gets injected into COSY with an injection energy of $78\,\mathrm{MeV}$. Within the first phase of the cycle the ion beam is accelerated until it has reached its final kinetic energy of $236\,\mathrm{MeV}$ and is bunched afterwards. After the acceleration the electron cooling of the ion beam is initiated by

turning on the electron current in the electron cooler. If electron and ion beam are adjusted correctly, the ion beam is now superimposed by the electron beam.

The superposition of both beams is done in the following way:

First the electron beam will be aligned to the center of the cooling section. By overlaying the electron gun voltage with an AC-signal the electron beam is becoming visible in the two beam position monitors in the cooling section of the cooler. With the corrector coils on the straight sections the electron beam can be aligned to the center of the cooler. Afterwards the ion beam will be aligned within the center of cooling section as well to overlap with the electron beam. The alignment is done with the help of four steerer magnets, two in front of the electron cooler and two behind (see figure 1.1). At this point it is important to mention that in order to be able to detect the recombined particles at the neutral particle detector it is vital to align both beams on axis in the center of the electron cooler, otherwise the recombined beam will not hit the extraction window at the end of the straight section of COSY, but rather gets lost before at the sidewalls of the vacuum pipe.

At initiation of electron cooling the total recombination rate is still low, but with further progress of the cooling it first drastically increases an then slowly flattens until reaching its maximum after a certain time. This behaviour of the total recombination rate can be explained with the help of the cross section for radiative recombination (see equation 2.17) that was already taken as a basis for the derivation of the recombination coefficient in subsection 2.3.1. The cross section states that for low relative energies between ions and electrons compared to the Rydberg energy the probability for an electron-ion pair to recombine in a certain Rydberg level n is proportional to $1/nE$. At the beginning of the cooling cycle, ions still have large energies relative to the electrons, which, following to the cross section, should lead to a low recombination rate. With further cooling the ions lose their energy via coulomb interaction with the electrons, which leads to a decrease of relative energy between ions end electrons and following to an increase of radiative recombination. One has to keep in mind that the electron temperature stays low, since the electron beam is permanently regenerated by the electron gun. At the end of the electron cooling, ions and electrons have reached the thermodynamic equilibrium meaning they have the same beam temperature and therefore ions will not be able to lose more thermal energy via coulomb interaction with the electrons. While the relative energy between ion and electrons reaches its minimum the recombination rate on the other hand reaches its maximum. At this point the cooling typically will be stopped, since no further improvement of the ion beam temperature can be reached.

5.2. Transverse Electron Temperature

Based on the recombination rate at flat top of the cooling cycle the transverse electron temperature can be calculated. While electron and deuteron beam do have the same temperature at the end of the cooling cycle, the velocity spread of the deuteron beam is much smaller than the of the electron beam. Following, one can consider

the deuterons in the beam as a resting target for the measurement of the transverse electron temperature. The ratio of the velocity spreads of the two beam is given by their mass ratio and amounts less than 2 %:

$$\frac{\Delta_i}{\Delta_e} = \sqrt{\frac{m_e}{m_i}}, \tag{5.1}$$

where Δ_i and Δ_e represent the velocity spread of the deuteron and electron beam respectively.

First one needs to express the theoretical expression of the recombination rate in measurable variables. Referring to A. Wolf *et al.* the following dependence between the total recombination rate R and the radiative recombination coefficient α_{rr} exists [47]:

$$R = \gamma^{-2} \eta N_i n_e \alpha_{rr}, \tag{5.2}$$

where η represents the fraction of the ion beam that on average is occupied by the electron beam. This value can be expressed by the ratio of the electron cooling section l_e to the ring circumference l_i. The effective cooling length of the 100 keV-Cooler amounts 2 m, whereas the storage ring has a circumference of 184 m. N_i and n_e denote the number of ions stored in the ring and the electron density in the electron beam, respectively. Since neither N_i nor n_e can be measured directly, one needs to express them by the ion beam current I_i and the electron beam current I_e. Making use of the definition of an electrical current, one finds:

$$I_e = \pi r_e^2 n_e \beta c e \quad \text{and} \quad I_i = l_i^{-1} N_e \beta c Z e. \tag{5.3}$$

Since a deuteron beam is used in this analysis, one can proceed with $Z = 1$. Applying equation 5.3 on equation 5.2 allows to express the recombination coefficient α_{rr} in dependence of the ion and electron beam current and the total recombination rate:

$$\alpha_{rr} = \frac{\pi r_e^2 c^2 \beta^2 \gamma^2}{l_e I_e I_i} R. \tag{5.4}$$

At COSY the ion beam current I_i is measured inductively via *fast current transformers* (FCT), whereas the electron beam current I_e is measured in the electron collector of the electron cooler. Both can be measured with very high resolutions. The FCTs at COSY do have a relative resolution of 0.2 % [44]. The error in the electron beam current is mainly caused by the loss of electrons in the electron cooler. The electron loss in the 100 keV-Cooler is below 0.5 % [41]. Therefore the errors that arise from the current measurements can be neglected in the error propagation and the error on the recombination coefficient just depends on the total recombination rate. The radiative recombination coefficient can be calculated to

$$\alpha_{rr} = (1.2 \pm 0.1) \cdot 10^{-13} \, \frac{\text{cm}^3}{\text{s}}. \tag{5.5}$$

In equation 2.25 an expression of the recombination coefficient α_{rr} as a function of the transverse temperature $kT_\perp$ was already given. After rearranging this equation one is able to determine the transverse temperature with knowledge of the recombination coefficient:

$$kT_\perp = 3.723 \cdot 10^{-24} \, \text{eV} \cdot \left(\frac{1}{\alpha_{rr} \left[\frac{\text{cm}^3}{\text{s}} \right]} \sum_{n=1}^{n_{max}} \frac{1}{n} \right)^2. \tag{5.6}$$

The error on the transverse temperature $\sigma_{kT_\perp}$ just depends on the error of the recombination coefficient $\sigma_{\alpha_{rr}}$ and can be determined by applying error propagation:

$$\sigma_{kT_\perp} = \sqrt{\left(\frac{\partial kT_\perp}{\partial \alpha_{rr}} \right)^2 \sigma_{\alpha_{rr}}^2} = 2kT_\perp \left(\alpha_{rr} \right) \cdot \frac{\sigma_{\alpha_{rr}}}{\alpha_{rr}}. \tag{5.7}$$

Finally one can calculate the transverse temperature

$$kT_\perp = \left(180 \pm 30 \right) \text{meV}. \tag{5.8}$$

The cathode of the electron gun has a temperature of approximately 1000°C. Electrons released by the cathode need to have the same temperature. 1000°C corresponds to an temperature of 110 meV in the energy scale. However, the measured transverse electron temperature is by 70 meV larger than the expected value.
Apparently the larger measured transverse electron temperature can be due to

1. a general misalignment of ion and electron beam,

2. a local misalignment caused by ripples in the magnetic guiding field or

3. a increase of the transverse electron temperature caused by ripples in the accelerating electric field of the electron gun.

During electron cooling the two beams have to be aligned in the way, that they travel parallel to each other with the same velocity. Machine restrictions or inaccurate monitoring of the beam alignment can cause a misalignment of the two beams to each other. Such a misalignment results in a small angle between the two beams.
A vector representation of this phenomenon is shown in figure 5.3. Assuming a perfectly aligned ion beam with the velocity $\vec{v}_i$ and an electron beam passing the cooling region with a small angle φ off axis and the velocity $\vec{v}_e$. Both beams do have the same absolute velocity v. The small angle produces a small transverse velocity component of the electron beam $v_{e\perp}$ relative to the ion beam:

$$v_{e\perp} = \sin(\varphi) \cdot v \approx \varphi \cdot v, \tag{5.9}$$

where the small-angle approximation $\sin(\varphi) \approx \varphi$ is used. The additional velocity component $\vec{v}_{e\perp}$ induces a shift of the Maxwell distribution of the electrons in the ion resting frame. The shifted two-dimensional Maxwell distribution is given by:
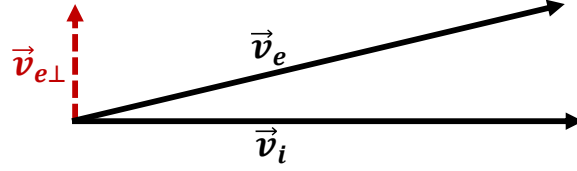
Figure 5.2.: Induced transverse velocity component $\vec{v}_{e\perp}$ caused by a misalignment of ion and electron beam

$$f(\vec{v}_\perp + \vec{v}_{e\perp}) = \frac{m_e}{2\pi kT_\perp} \exp\left(-\frac{m_e(\vec{v}_\perp + \vec{v}_{e\perp})^2}{2kT_\perp}\right). \tag{5.10}$$

Following the equipartition principle the average kinetic energy of a gas in two dimensions is given by its temperature:

$$\langle E_{kin}\rangle_{f(\vec{v}_\perp)} = \int_0^\infty \frac{1}{2} m_e v_\perp^2 f(\vec{v}_\perp) dv_\perp = kT_\perp. \tag{5.11}$$

If one wants to determine the average kinetic energy in consideration of the additional velocity component, one needs to calculate the average with respect to the shifted Maxwell distribution:

$$\langle E_{kin}\rangle_{f(\vec{v}_\perp + \vec{v}_{e\perp})} = \int_0^\infty \frac{1}{2} m_e v_\perp^2 f(\vec{v}_\perp + \vec{v}_{e\perp}) dv_\perp = kT_\perp + E_{e\perp}. \tag{5.12}$$

A derivation of equation 5.12 can be found in section A.4. The increase of the average kinetic energy resulting in a transverse electron temperature increase in the measurements is a quadratic function of the angle φ between ion and electron beam directory:

$$\Delta kT_\perp = E_{e\perp} = \varphi^2 E_e, \tag{5.13}$$

where E_e denotes the absolute kinetic energy of the electrons. Considering an angle of 0.5 mrad, such an angle corresponds to an offset of the beam after passing the cooling section by 1 mm, for an electron beam energy of 100 keV this would lead to an increase of the measured transverse temperature of 25 meV. For an operation at the lower energy of 24.5 keV the above mentioned angle would cause a significantly lower transverse electron temperature shift of 6 meV.

A second effect can induce a local misalignment of the electron beam relative to the ion beam caused by ripples in the magnetic guiding field in the cooling section. Measurements have shown that the magnetic field created by the drift-solenoid is not a straight line, but is rather bend to the upper left. A short description of the measurement technique and results can be found in section A.3.

The origin for the bending of the guiding field lies in the heating-up of the drift-solenoid. Through the thermal expansion of the copper of the solenoid coils the
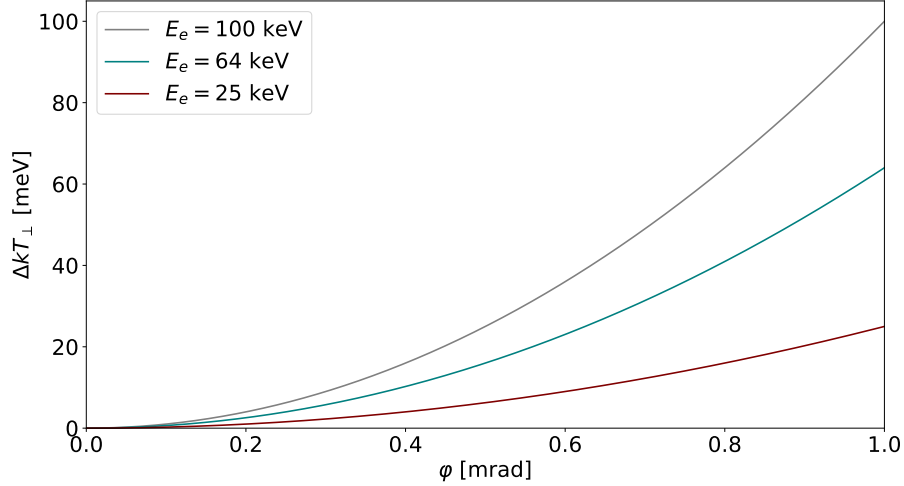
Figure 5.3.: Increase of the measured temperature $\Delta kT_\perp$ as a function of the angle φ for different kinetic electron energies E_e

length of the solenoid increases slightly. However, the current installation does not allow a linear expansion of the cooling solenoid, by what the solenoid gets bend.
This causes a bending of the solenoid field that varies between $-0.1\,\mathrm{mrad}$ and $0.4\,\mathrm{mrad}$. Since the electrons are following the guiding solenoid field, the trajectory of the electron beam experiences a bending as well. Nevertheless the ion beam is not influenced by the magnetic field and will follow its trajectory. The same considerations that were taken above for a general misalignment of the beam can also be applied in this case. The bending of the solenoid field causes an local increase of transverse electron temperature of up to $16\,\mathrm{meV}$ at an kinetic energy of $100\,\mathrm{keV}$.
Assuming many-body effects like electron-electron repulsion repulsion are neglectable, there are still single particle effects that can increase the transverse temperature of the electrons during their trajectory trough the cooler.
One already occurs during the acceleration of the electrons. At the end of the acceleration tube transverse electric fields can not be avoided. Such a defocussing field leads to an increase of the transverse electron temperature since they increase the velocity of the electrons transverse to the beam direction [2].
During the design of the $100\,\mathrm{keV}$-Cooler simulations of the electric field in the acceleration tubes were already carried out in order to minimize the transverse electric field and therefore the heating of the electron beam with a well chosen design of the electron gun. Nevertheless small local transverse fields can not be avoided. Following to the results of the field calculation a transverse electric field of less than $6\,\mathrm{kV/cm}$ can be reached. A transverse acceleration of the electrons forces them on larger Lamor radii and therefore increases the transverse electron temperature.

6. Summary

The here presented work dealt with the process of radiative recombination during electron cooling of proton and deuteron beams at the COSY storage ring. Electron cooling is an useful method to shrink the emittance of a beam needed for high precision experiments. For the present recombination studies the 100 keV-Cooler at COSY was utilized. In principle one could carry out the same experiments with the 2 MeV-Cooler as well. Unfortunately, problems with the centering of the ion beam within the electron cooler prevent the recombined particles to be detected in the neutral particle detector reliably.

Since the radiative recombination just depends on the energy of the electrons in the ion-resting-frame, which on average can be expressed by the transverse temperature of the electron beam, the analysis recombination rates during the cooling process is a useful method to study the transverse temperature of the electron beam.

The transverse electron temperature is defined by the temperature of the electron cathode. It has been shown, that a misalignment of ion and electron beam induces a shift of the Maxwell distribution to higher velocities, which leads to an increase of the average kinetic energy in the ion-resting-frame and thus to an increase of the measured transverse electron temperature. In a first approximation, knowing the cathode temperature one could in principle calculate the angle between ion and electron beam directory. In addition ripples in the accelerating electric field and the guiding magnetic field can contribute to a heating-up of the electron beam as well as to a locally enhanced misalignment.

For the operator of the electron cooler in order to optimize the cooling with respect to the beam alignment a real-time analysis and monitoring of the recombination rate and electron temperature is highly valuable. Using the Red Pitaya STEMLab board a fully digital signal processing and acquisition system has been developed and putted into operation. For this purpose a custom FPGA firmware has been developed that uses a threshold crossing technique for pulse detection. Integration of the acquired data into the EPICS control system allows real-time access as well as archiving. The EPICS integration was made possible by a modified EPICS IOC that is able to communicate with the FPGA. Finally a web monitoring system has been provided to visualize the acquired data in real-time.

7. Outlook

In section 5.2 the transverse electron temperature based on the recombination rate was studied. As an improvement of the transverse electron temperature one could in principal make use of adiabatic expansion of the electron beam to cool at lower transverse electron temperatures and improve the cooling performance. A theoretical description of adiabatic beam expansion was already given in subsubsection 2.2.2.1. Currently a current of 364 A is applied to the cooler magnets offering a guiding field strength of 50 mT. The water cooling of the magnets and the power supplies though are designed for a maximal current of 960 A offering a guiding field strength of 132 mT. Theoretically one could therefore expand the electron beam by a factor of B_c/B = 2.6 by applying the maximal current to the gun- and collector-solenoid while keeping the toroids and the cooling-solenoid at the well the established current of 364 A.

The *Max-Planck-Institute for Nuclear Physics* successfully carried out recombination based transverse electron temperature studies with the electron cooler at the TSR heavy ion storage ring [20]. Their experimental results are in good agreement with the theoretical considerations for the ions C^{6+} and F^{6+} in the low energy range. Nevertheless electron coolers as the one used at the TSR are specially designed to make use of adiabatic beam expansion. Such electron coolers consist of two solenoids in series on the straight section of the electron gun. By applying a higher current to the first solenoid, which surrounds the electron gun and a lower current to the second solenoid, one is able to let the adiabatic expansion take place smoothly before entering the toroids guiding the electron beam into the cooling section.

The 100 keV-Cooler at COSY originally was not designed to expand the electron beam adiabatically, since it has only one solenoid on the straight section of the electron gun. As a result one has to expand the electron beam either at the transition from the gun-solenoid to the 35°-toroid or at the transition from the 35°-toroid to the 55°-toroid. The latter has already been tried out, without any success so far, because one was not able to control the electron beam any longer. Furthermore the gateway of the higher guiding field seems to have a not negligible influence on the ion beam. Considering these arguments the first approach seems more promising.

7.1. Adiabatic Expansion of the Electron Beam

In order to study the feasibility of adiabatic expansion in the 100 keV-Cooler simulations were carried out. For this purpose the *MagWire* framework, a python framework for magnetostatic simulations of simple current-carrying conductors, was taken as a basis and developed further [26]. The MagWire framework uses finite element simu-

lation by exploiting the *Law of Biot-Savart* to calculate the magnetic field caused by a finite current-carrying conductor. Geometric data of the magnets was taken from the original construction plans of the 100 keV-Cooler. To ensure that the simulated magnetic field resamples the real magnetic field created by the cooler magnets a simulation without adiabatic expansion was carried out and compared to the simulation results of J. G. de Villiers *et al.* [37]. They already did a numerical field analysis in the year 2013 in order to study the distortion of the ion beam trajectory caused by the field of the cooler magnets.

After calculating the three-dimensional field map of the guiding field one can determine the path the electrons are following. This is typically done by finding the field lines of the guiding field. The field lines of an arbitrary vector field are simply defined as the tangent to each field vector in space along its own length. By following the field lines going through the center of the gun-solenoid one finds the path, which the electrons in theory are following through the electron cooler.

Afterwards one can extract the field strength of the guiding field at each point on the electron trajectory by calculating the euclidean norm of the vector field. Finally the adiabaticity coefficient can be calculated numerically making use of equation 2.14. A schematic of the simulated structure can be seen in figure 7.1. Due to computational limitations only the first part of the electron cooler up to the middle of the cooling section was simulated.
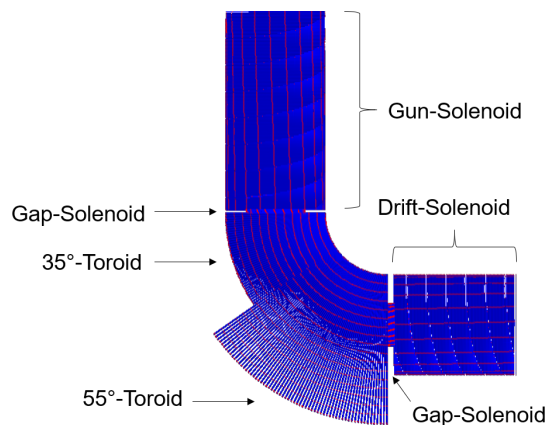
Figure 7.1.: Simulated structure of the 100 keV-Cooler

Several simulations for different expansion factors were carried out. In figure 7.2 the adiabaticity coefficient as well as the magnetic field strength along the electron trajectory for the maximal feasible expansion factor of 2.6 is shown. To reduce the gateway of the higher gun-solenoid field the gap-solenoid between gun-solenoid and 35°-toroid was turned off in this simulation.

It can clearly be seen, due to the missing field of the gap-solenoid the field strength drops by 41 mT from the center to the end of the gun-solenoid down to 91 mT. This means half of the beam expansion can already take place within the straight section of the gun-solenoid. The adiabaticity coefficient reaches his maximum at the transi-
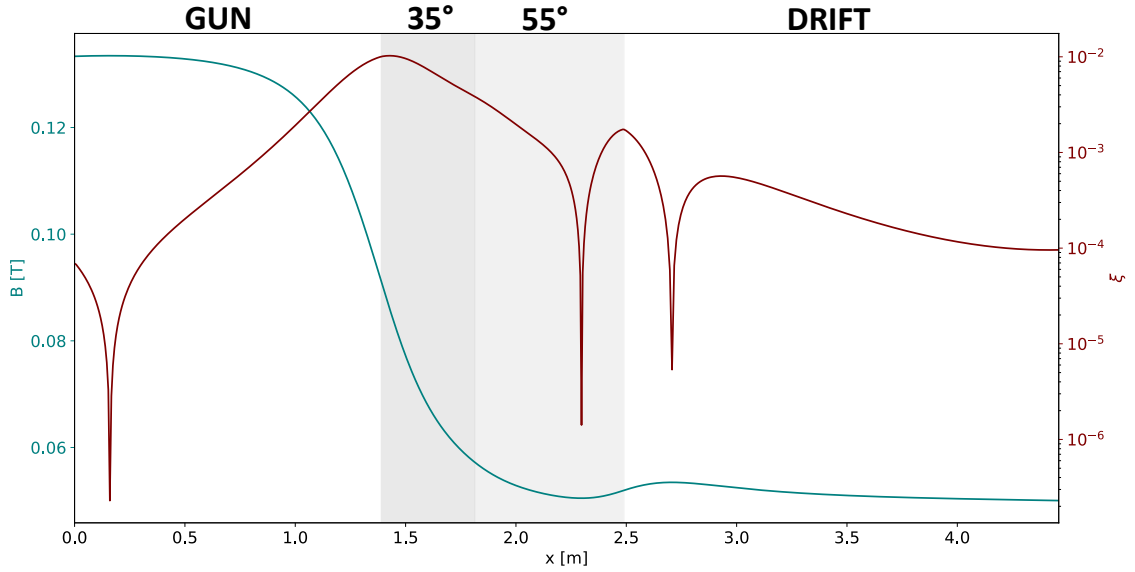
Figure 7.2.: Magnetic field strength and adiabaticity coefficient along the electron trajectory at a kinetic energy of 100 keV

tion to the 35°-toroid. Since the maximal adiabaticity coefficient of 0.01 fulfils the adiabaticity condition, the expansion of the beam still remains adiabatically at this point (see subsubsection 2.2.2.1).

The remaining expansion takes place within the curvature of the 35°-toroid. The field strength in the small toroid section decreases down to 57 mT and afterwards reaches his minimum of 50 mT in the center of the 55°-toroid. Therefore only a small part of the larger gun-solenoid field continues to the region where the electron and ion beam overlap, keeping the impact of the larger field on the ion beam as small as possible. Besides small deflections from the ideal ion trajectory are expected to be corrected with the help of the steerer magnets in front of the electron cooler.

First experiments without ion beam have successfully been carried out trying to control the expanded electron beam. It has been seen that the larger field of the gun-solenoid leads to a vertical downshift of the electron trajectory. However, the downshift can be corrected with the Helmholtz coils surrounding the straight section of electron gun (see section 1.2). Next to an improvement of the electron cooling performance, an expansion of the electron beam also promises to reduce the so called *initial losses* at COSY.

7.2. Initial Losses

As it was mentioned before, at COSY there are two possibilities to initiate the electron cooling of the ion beam. In the first case, the ion beam will be cooled directly after injection into the storage ring. In the second case, the beam first will be accelerated and then be cooled after bunching. Either way large losses of particles can be expected. In the latter mode of operation losses already occur during the bunching the beam. Afterwards the beam can be cooled lossless. The more interesting mode of operation for the current discussion of adiabatic expansion is the first one, in which the ion beam is cooled directly after injection.
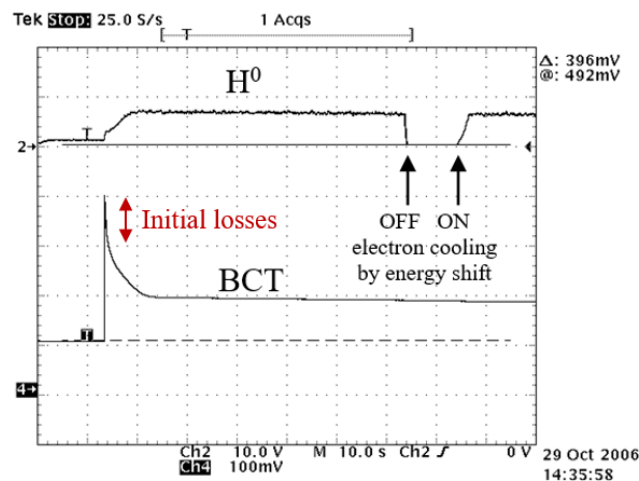
Figure 7.3.: Oscilloscope recording of the recombination rate and ion beam current at electron cooling after injection [41]

Initial losses can be observed at the beginning of the beam cooling. These kind of losses have been tried to be understood in detail for several years. Since no betatron oscillations can be seen during the cooling of the beam, the initial losses have to be of incoherent nature. The explanation that came to be seen the most viable, is the following:
After injection the ion beam is filling the whole ring acceptance of COSY. Thus the ion beam has a significantly larger diameter than the electron beam of the $100\,\mathrm{keV}$-Cooler. Only the ions in the beam center are in superposition with the electron beam and will be cooled. The electric field outside the electron beam decreases with $1/r^2$, with r being the distance from the edge of the electron beam. This non-linear electric field containing higher multipoles may excite non-linear resonances, which finally will cause the initial losses [21]. Experiments supporting the upper assumptions have shown an increase of the initial losses at higher electron currents. A higher electron current at constant electron energy implies an denser electron beam. The higher the electron density the higher the outer electric field, which leads to an amplification of non-linear resonances.

With adiabatic beam expansion one in theory is able to enlarge the electron beam radius by an factor of 1.6 following to equation 2.15. Thereby a significantly larger part of the ion beam will be in superposition with the electron beam and therefore be cooled. Finally this will lead to a weakening of initial losses.

Bibliography

[1] A. Uchiyama et al. "EPICS channel access using Websocket". In: *Proceedings of PCaPAC2012* (2012).

[2] M. I. Bryzgunov et al. "Calculation of electron beam motion in electron cooling system for COSY". In: *ECOOL* (2009).

[3] L. H. Andersen and J. Bolko. "Radiative recombination between fully stripped ions and free electrons". In: *Physical Review A* (1990).

[4] *Archiver Homepage.* 2019-06-05. URL: https://slacmshankar.github.io/epicsarchiver_docs/.

[5] I. Bekman et al. "Experience and Prospects of Real-Time Signal Processing and Representation for the Beam Diagnostics at COSY". In: *ICALEPCS* (2018).

[6] M. Bell and J. S. Bell. "Capture of cooling electrons by cool protons". In: *Part. Accel.* (1981).

[7] H. A. Bethe and E. E. Salpeter. "Quantum Mechanics of One and Two Electron Systems". In: *Annalen der Physik* (1957).

[8] G. I. Budker. "An effective method of damping particle oscillations in proton and antiproton storage rings". In: *Soviet Atomic Energy* (1967).

[9] *CAEN AG7435 Documentation.* 2019-06-05. URL: https://www.caen.it/products/ag7435/.

[10] *CAEN SY5527lC Documentation.* 2019-06-05. URL: https://www.caen.it/products/sy5527lc/.

[11] *Control System Studio Homepage.* 2019-07-25. URL: http://controlsystemstudio.org/.

[12] J. H. Conway. *Regular Algebra and Finite Machines.* Dover Pubications, 2012.

[13] *D3 Homepage.* 2019-07-24. URL: https://d3js.org/.

[14] *Docker Homepage.* 2019-07-24. URL: https://www.docker.com/.

[15] *Documentation of the WebSocket Protocol.* 2019-07-25. URL: https://tools.ietf.org/html/rfc6455.

[16] *Encyclopaedia entry about photomultiplier tubes.* 2019-06-05. URL: https://en.wikipedia.org/wiki/Photomultiplier_tube.

[17] *Encyclopaedia entry about wire chambers.* 2019-06-05. URL: https://en.wikipedia.org/wiki/Wire_chamber.

[18] *EPICS Homepage.* 2019-06-05. URL: https://epics-controls.org/.

[19] *EPICS Interface for JavaScript.* 2019-07-24. URL: https://github.com/RobbieClarken/node-epics.

[20] G. Gwinner et al. "Influence of magnetic fields on electron-ion recombination at very low energies". In: *Physical review letters* (2000).

[21] *H. J. Stein (internal communication).*

[22] G. I. Budker et al. "Experimental Studies Of Electron Cooling". In: *Experimental Study of Electron Cooling (transl. into English from Russian paper)* (1976).

[23] H. A. Kramers. "On the theory of X-ray absorption and of the continuous X-ray spectrum". In: *The London, Edinburgh, and Dublin Philosophical Magazine and Journal of Science* (1923).

[24] *Lecture script on radioisotopes and radiation methodology.* 2019-06-05. URL: https://www.science.mcmaster.ca/radgrad/images/6R06CourseResources/4R6Notes4_ScintillationDetectors.pdf.

[25] W. R. Leo. *Techniques for Nuclear and Particle Physics Experiments: A How to Approach.* 1987.

[26] *MagWire Documentation.* 2019-06-05. URL: https://www.geophysik.uni-muenchen.de/~wack/teaching/Python/6_magwire.html.

[27] *Node.js Homepage.* 2019-07-24. URL: https://nodejs.org/.

[28] M. Pajek and R. Schuch. "Total radiative recombination rates for ions interacting with electrons from an electron cooler". In: *Nuclear Instruments and Methods in Physics Research Section B: Beam Interactions with Materials and Atoms* (1994).

[29] V. V. Parkhomchuk and A. N. Skrinsky. "Electron cooling: physics and prospective applications". In: *Reports on Progress in Physics* (1991).

[30] H. Poth. "Electron cooling: theory, experiment, application". In: *Physics reports* (1990).

[31] *Red Pitaya Documentation - 3.1.1. STEMlab 125-10 vs. STEMlab 125-14.* 2019-06-05. URL: https://redpitaya.readthedocs.io/en/latest/developerGuide/125-10/vs.html.

[32] *Red Pitaya Documentation - 3.1.3. STEM 125-14.* 2019-06-05. URL: https://redpitaya.readthedocs.io/en/latest/developerGuide/125-14/top.html.

[33] *Red Pitaya Github Repository.* 2019-06-05. URL: https://github.com/RedPitaya.

[34] W. Schwab. "Experimente zur Elektronenkühlung am Niederenergie-Antiprotonen-Speicherring (LEAR)". PhD Thesis. KIT, 1990.

[35] J. Serrano. "Introduction to FPGA design". In: *CERN Accelerator School* (2008).

[36] *Socket.io Homepage.* 2019-07-24. URL: https://socket.io/.

[37] H. Soltner et al. "Three-Dimensional Numerical Field Analysis for the Magnets of the 100-keV Electron Cooler at COSY-Jülich". In: *IEEE Transactions on Applied Superconductivity* (2014).

[38] M. Steck. *Presentation on Beam Cooling.* 2009. URL: https://cas.web.cern.ch/sites/cas.web.cern.ch/files/lectures/darmstadt-2009/steck.pdf.

[39] M. Stobbe. "Zur Quantenmechanik photoelektrischer Prozesse". In: *Annalen der Physik* (1930).

[40] J. Su. "Design and Development of an FPGA-based Distributed Computing Processing Platform". In: *Bucknell Digital Commons* (2011).

[41] *The COSY Electron Cooler and the COSY Ring (internal Note).*

[42] *umweltanalyse.com.* 2019-06-05. URL: https://www.umweltanalysen.com/radioaktivitaet/caesium-137/.

[43] S. Usman and A. Patil. "Radiation detector deadtime and pile up: A review of the status of science". In: *Nuclear Engineering and Technology* (2018).

[44] Y. Valdau et al. "Development of High Resolution Beam Current Measurement System for COSY-Julich". In: *Proceedings, 5th International Beam Instrumentation Conference* (2017).

[45] *Verilog Documentation.* 2019-06-05. URL: http://www.verilog.com/.

[46] *VHDL Documentation.* 2019-06-05. URL: https://vhdlguide.readthedocs.io/en/latest/#.

[47] A. Wolf et al. "Recombination in electron coolers". In: *Nuclear Instruments and Methods in Physics Research Section A: Accelerators, Spectrometers, Detectors and Associated Equipment* (2000).

A. Appendix

A.1. Calculation of the vertical Toroid Field

Measurements of the strength of the vertical magnetic field in the toroid region of the 100 keV Cooler were carried out with the help of a *Hall Effect Sensor.* The Sensor was passed through the toroid magnet on axis at an magnetic guiding field of 120 mT (1200 Gs).
The maximum field strength measured with the sensor is in good agreement with the theoretical value that can be calculated using the formula of a magnetic field created by a toroid magnet. It states that the vertical component on axis is half as large as the total strength of the guiding field.
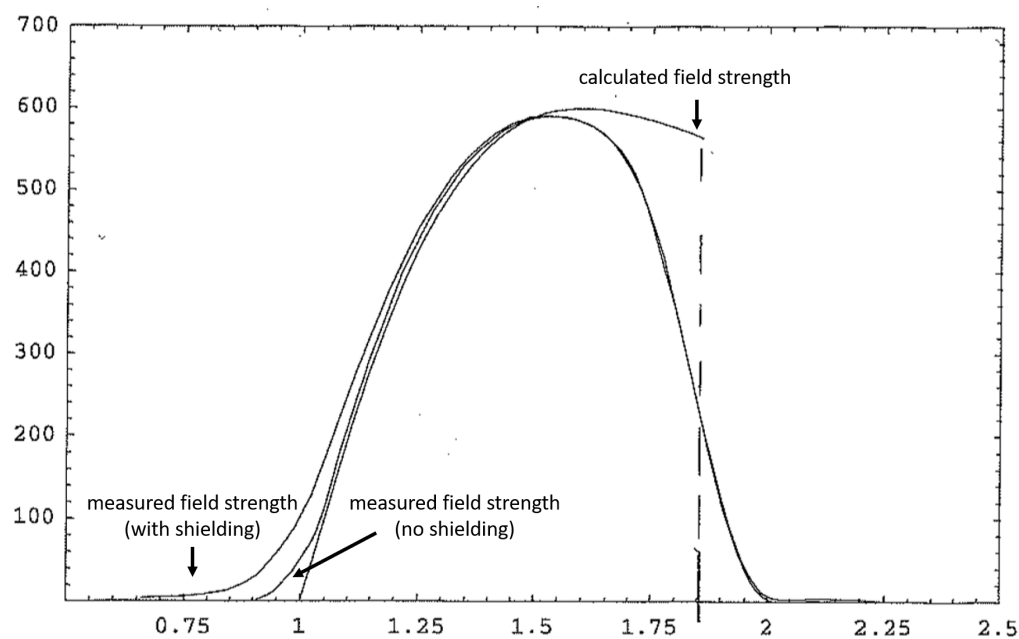
Figure A.1.: Comparison of the Measurements and Calculation of the vertical toroid field [21]

A.2. Calibration of High Voltage Supply

In order to find the stable region of operation, the high voltage has been varied between 1700 V and 2150 V. Measurements have been taken with a radioactive source *Caesium-137*. It has a half-life of 30.17 years and decays by beta emission into the stable *Barium-137* [42]. Besides measurements without radioactive source were taken as well. It can be seen, in the whole high voltage range that has been scanned one is able to clearly distinguish between noise and the beta decay of the radioactive source.
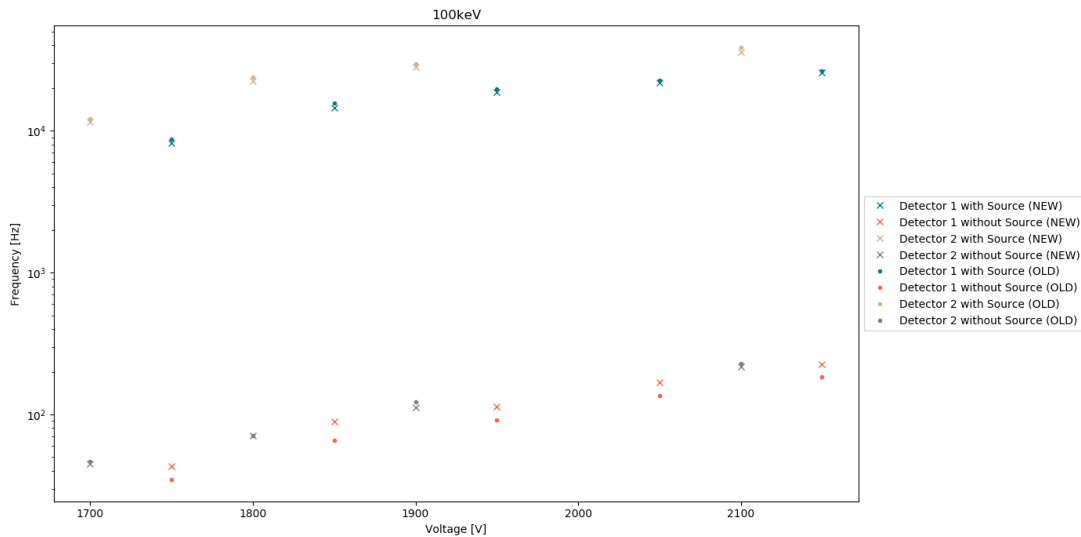
Figure A.2.: Measurement of photomultiplier output at different high voltages between 1700 V and and 2150 V

A.3. Measurements of the Guiding Field Lines in the Cooling Region

Small transverse components of the guiding field in the cooling region were measured by a magnetic needle made out of iron. Within the magnetic field the needle is directed along the magnetic field lines if supported by a bearing that allows the free alignment in the two transverse directions. The field direction can be measured by an electronic autocollimation system using a mirror attached to the iron needle. The autocollimator sends a parallel beam of light onto the mirror. In equilibrium the mirror is perpendicular to the beam reflecting the light along the same path. When the mirror is tilted due to a transverse component in the magnetic guiding field, the light is reflected with a certain angle. From the distance between the reflected image to the light source, one is able to determine the angle by which the mirror is tilted and therefore the angle of the magnetic field.
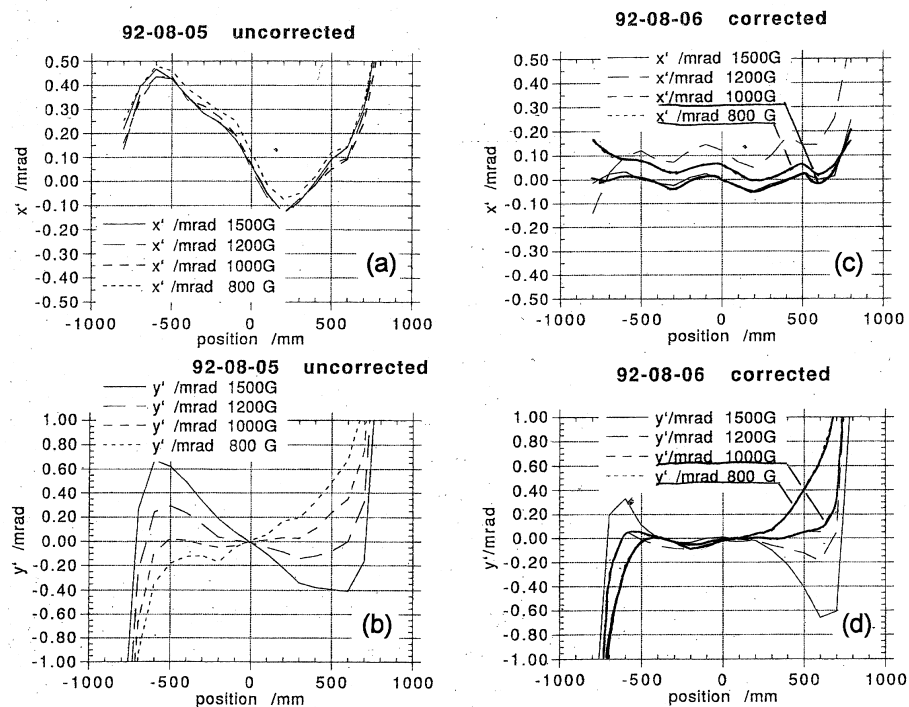
Figure A.3.: Measurements of the magnetic field line angles along the drift solenoid, (a) and (b) the horizontal (x) and vertical (y) field angles of the solenoid as it was manufactured, (c) and (d) after appropriate correction using saddle coils with varying azimuthal angle [41]

A.4. Derivation of transverse Temperature shift

In order to derive an equation for the increase of the measured transverse temperature that is caused by an additional velocity component, one can assume a electron gas moving on a two-dimensional plane with the temperature kT. The additional velocity component $\vec{w}$ induces a shift of the two-dimensional Maxwell distribution:

$$
\begin{aligned}
f_{\mathrm{2D}}(\vec{v} + \vec{w}) &= \frac{m_e}{2\pi kT} \exp\left(-\frac{m_e(\vec{v} + \vec{w})^2}{2kT}\right) \\
&= \frac{m_e}{2\pi kT} \exp\left(-\frac{m_e(v_x + w_x)^2}{2kT} - \frac{m_e(v_y + w_y)^2}{2kT}\right).
\end{aligned}
$$

The transverse temperature shift can be derived by calculating the average of the kinetic energy E_{kin} with respect to the shifted Maxwell distribution:

$$
\begin{aligned}
&\langle E_{kin}\rangle_{f_{\mathrm{2D}}(\vec{v}+\vec{w})} \\
&= \int_{-\infty}^{\infty} d^2v \, \frac{1}{2} m_e \vec{v}^2 \, f_{\mathrm{2D}}(\vec{v} + \vec{w}) \qquad\qquad\qquad (\text{substitute } \vec{u} = \vec{v} + \vec{w}) \\
&= \int_{-\infty}^{\infty} d^2u \, \frac{1}{2} m_e (\vec{u} - \vec{w})^2 \, f_{\mathrm{2D}}(\vec{u}) \\
&= \int_{-\infty}^{\infty} d^2u \, \frac{1}{2} m_e (\vec{u}^2 + \vec{w}^2 - 2\vec{u}\vec{w}) \, f_{\mathrm{2D}}(\vec{u}) \\
&= \underbrace{\int_{-\infty}^{\infty} d^2u \, \frac{1}{2} m_e \vec{u}^2 \, f_{\mathrm{2D}}(\vec{u})}_{=kT} + \int_{-\infty}^{\infty} d^2u \, \frac{1}{2} m_e \vec{w}^2 \, f_{\mathrm{2D}}(\vec{u}) - \int_{-\infty}^{\infty} d^2u \, m_e \vec{u}\vec{w} \, f_{\mathrm{2D}}(\vec{u}) \\
&= kT + \frac{1}{2} m_e \vec{w}^2 \underbrace{\int_{-\infty}^{\infty} d^2u \, f_{\mathrm{2D}}(\vec{u})}_{=1} - m_e \int_{-\infty}^{\infty} d^2u \, \vec{u}\vec{w} \, f_{\mathrm{2D}}(\vec{u}) \\
&= kT + \underbrace{\frac{1}{2} m_e \vec{w}^2}_{=E_w} - m_e \int_{-\infty}^{\infty} d^2u \, \vec{u}\vec{w} \, f_{\mathrm{2D}}(\vec{u}) \\
&= kT + E_w - m_e w_x \underbrace{\int_{-\infty}^{\infty} d^2u \, u_x \, f_{\mathrm{2D}}(\vec{u})}_{=\langle u_x\rangle = 0} - m_e w_y \underbrace{\int_{-\infty}^{\infty} d^2u \, u_y \, f_{\mathrm{2D}}(\vec{u})}_{=\langle u_y\rangle = 0} \\
&= kT + E_w.
\end{aligned}
$$